

Sparsity-driven Coupled Imaging and Autofocusing for Interferometric SAR

by Oğuzcan Zengin

Submitted to the Graduate School of Sabancı University
in partial fulfillment of the requirements for the degree of
Master of Science

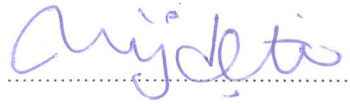
Sabancı University

July, 2018

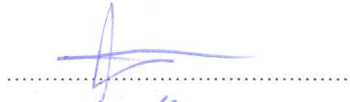
SPARSITY-DRIVEN COUPLED IMAGING AND AUTOFOCUSING FOR
INTERFEROMETRIC SAR

APPROVED BY

Assoc. Prof. Dr. Müjdat Çetin
(Thesis Supervisor)



Assoc. Prof. Dr. Kemal Kılıç



Assist. Prof. Dr. N. Özben Önhon



DATE OF APPROVAL: 31.07.2018

© Oğuzcan Zengin 2018
All Rights Reserved

SPARSITY-DRIVEN COUPLED IMAGING AND AUTOFOCUSING FOR INTERFEROMETRIC SAR

Oğuzcan Zengin

EE, M.Sc. Thesis, 2018

Thesis Supervisor: Assoc. Prof. Müjdat Çetin

Keywords: Synthetic Aperture Radar, Regularization-based imaging, Joint Sparsity, Model errors, Phase errors, Autofocus, SAR Interferometry

Abstract

In this thesis, we present a new joint image enhancement and reconstruction method and a software processing tool for SAR Interferometry. First, we propose a sparsity-driven method for coupled image formation and autofocusing based on multi-channel data collected in interferometric synthetic aperture radar (IfSAR). Relative phase between SAR images contains valuable information. For example, it can be used to estimate the height of the scene in SAR Interferometry. However, this relative phase could be degraded when independent enhancement methods are used over SAR image pairs. Previously, Ramakrishnan, Ertin, and Moses proposed a coupled multi-channel image enhancement technique, based on a dual descent method, which exhibits better performance in phase preservation compared to independent enhancement methods. Their work involves a coupled optimization formulation that uses a sparsity enforcing penalty term as well as a constraint tying the multichannel images together to preserve the cross-channel information. In addition to independent enhancement, the relative phase between the acquisitions can be degraded due to other factors as well, such as platform location uncertainties, leading to phase errors in the data and defocusing in the formed imagery. The performance of airborne SAR systems can be affected severely by such errors. We

propose an optimization formulation that combines Ramakrishnan et al.'s coupled IfSAR enhancement method with the sparsity-driven autofocus (SDA) approach of Önhon and Çetin to alleviate the effects of phase errors due to motion errors in the context of IfSAR imaging. Our method solves the joint optimization problem with a Lagrangian optimization method iteratively. In our preliminary experimental analysis, we have obtained results of our method on synthetic SAR images and compared its performance to existing methods. As a second contribution of this thesis, we have developed a software toolbox for end-to-end interferometric SAR processing. This toolbox is capable of performing the fundamental steps of SAR Interferometry Processing. The thesis contains the detailed explanation of the algorithms implemented in the SAR Interferometry Toolbox. Test results are also provided to demonstrate the performance of the Toolbox under different scenarios.

INTERFEROMETRİK SAR İÇİN SEYREKLİK-ODAKLI ORTAK GÖRÜNTÜLEME VE ODAKLAMA

Oğuzcan Zengin

EE, Yüksek Lisans Tezi, 2018

Tez Danışmanı: Doç. Dr. Müjdat Çetin

Anahtar Kelimeler: Sentetik Açıklıklı Radar, Düzenlileştirmeye dayalı görüntü oluşturma, Ortak Seyreklik, Model hataları, Faz hataları, Otomatik odaklama, SAR Interferometrisi

Özet

Bu tezde, yeni bir düzenlileştirmeye dayalı görüntü oluşturma yöntemi ve SAR İnterferometrisi için bir yazılım işleme aracı sunduk. İlk olarak, interferometrik sentetik açıklıklı radarda (IfSAR) toplanan çok kanallı verilere dayanarak, eşleşmiş görüntü oluşumu ve otomatik odaklama için bir yöntem önermekteyiz. SAR görüntüleri arasındaki göreceli faz değerli bilgiler içerir. Örneğin, SAR İnterferometrisinde sahnenin yüksekliğini tahmin etmek için kullanılabilir. Bununla birlikte, SAR görüntü çiftleri üzerinde bağımsız iyileştirme yöntemleri kullanıldığında, bu nispi faz bozulabilir. Daha önce, Ramakrishnan, Ertin ve Moses, bağımsız iyileştirme yöntemleri ile karşılaştırıldığında, faz korunmasında daha iyi başarımlar sergileyen ikili bir iniş yöntemine dayanan, birleşik çok kanallı görüntü geliştirme tekniğini önermişlerdir. Çalışmaları, çapraz-kanal bilgisini korumak için çok kanallı görüntüleri birbirine bağlayan bir kısıtlamanın yanı sıra bir seyreklik cezası terimi kullanan birleştirilmiş bir eniyileme kurgusu içermektedir. Bağımsız iyileştirmeye ek olarak, görüntüler arasındaki göreceli faz, platform konum belirsizlikleri, verilerin faz hatalarına yol açması ve oluşan görüntülerde bulanıklaştırma gibi diğer faktörlere bağlı olarak da bozulabilir. SAR sistemlerinin başarımlarını, bu tür hatalardan ciddi şekilde

etkilenebilir. Ramakrishnan ve Ertin'in ortak seyreklik odaklı IfSAR görüntü oluşturma yöntemini, Önhon ve Çetin'in seyreklik odaklı odaklama (SDA) yaklaşımı ile birleştirerek, IfSAR görüntüleme bağlamında hareket hatalarından kaynaklanan faz hatalarının etkilerini hafifletmek için bir eniyileme kurgusu öneriyoruz. Bizim yöntemimiz, ortak eniyileme problemini yinelemeli olarak Lagrange eniyileme yöntemiyle çözmektedir. Ön deneysel analizimizde, sentetik SAR görüntüleri üzerinde yöntemimizin sonuçlarını elde ettik ve performansını mevcut yöntemlerle karşılaştırdık. Bu tezin ikinci katkısı olarak, SAR İnterferometrisi için bir yazılım aracı geliştirdik. Bu araç, SAR İnterferometrisi işlem sürecinin temel adımlarını gerçekleştirebilecek şekilde tasarlanmıştır. Son ürün olarak görüntülenen alanın 3 boyutlu bir modelini oluşturabilir. Bu tezde, SAR İnterferometry Algoritması'nda uygulanan algoritmaların detaylı açıklaması verilmiştir. Ayrıca, Algoritma'nın test sonuçları, Algoritma'nın başarısını farklı senaryolar altında gösterecek şekilde tanıtılmıştır.

Acknowledgements

Firstly, I would like to express my sincere gratitude to my advisor Dr. Müjdat Çetin for the continuous support of my M.Sc. study and related research, for his patience, motivation, and immense knowledge. His guidance helped me in all the time of research and writing of this thesis. I could not have imagined having a better advisor and mentor for my M.Sc. study.

My sincere thanks also goes to Dr. Ahmed Shaharyar Khwaja, who provided his support and vision. Without their precious support it would not be possible to conduct this research.

Besides my advisor, I would like to thank the rest of my thesis committee: Dr. Kemal Kılıç, Dr. Özben Önhon for their insightful comments and encouragement, but also for the hard question which incited me to widen my research from various perspectives.

I thank my dear friends Ece Aydın, İpek Baz, Emre Can Durmaz, Majed Elwardy, Elif Melis Enç, Abdullah Göktuğ Gönel, Sezen Yağmur Günay, Aykut Önal, Emre Özçelik, Ozan Özdenizci, Başak Tavşanoğlu, Esra Yüksel in for the stimulating discussions, for the sleepless nights we were working together before deadlines, and for all the fun we have had in the last four years.

Then, I would like to thank my family for supporting me spiritually throughout my life in general.

Contents

1	Introduction	1
1.1	Motivation	1
1.2	Contribution of the Thesis	4
1.3	Organization of the Thesis	5
2	Preliminaries	7
2.1	Synthetic Aperture Radar	7
2.1.1	Spotlight SAR Imaging Model	8
2.1.2	Conventional Image Formation Algorithms	12
2.1.3	SAR Autofocus Problem	12
2.2	SAR Interferometry	15
2.2.1	Image Resolution Quality Measurements	15
2.2.2	Examples of Operational IfSAR Satellite Systems	16
2.2.3	Principles of Interferometry	19
2.2.4	Fundamentals of SAR Interferometry	20
2.2.5	SAR Interferometry Baseline Problem	25
2.3	Regularization Based Image Reconstruction	29
2.3.1	Non-Quadratic Regularization	30
2.3.2	Joint Enhancement Problem in IfSAR	31

3	Sparsity-driven Coupled Imaging and Autofocusing for Interferometric SAR	33
3.1	Introduction	33
3.2	Proposed Method	35
3.2.1	Updating the Images	37
3.2.2	Updating the Phases and the Observation Matrices	39
3.3	Simulation Results	42
4	SAR Interferometry Toolbox Project	57
4.1	Project Description	57
4.2	SAR Interferometry Toolbox	58
4.2.1	Algorithm Design	59
4.2.2	SAR Interferometry Toolbox GUI	68
4.2.3	Toolbox Outputs	68
4.2.4	Tests and Analyses	71
5	Conclusion	94
5.1	Summary	94
5.2	Potential Research Directions	95
5.2.1	Testing SDCIA on a real world scenario	95
5.2.2	Extension of SDCIA to more than two channels	95
5.2.3	Application of the Proposed Method to other domains	96
A		97

List of Figures

1.1	Simple illustration of SAR imaging operation. Image is taken from the web site of Sandia National Laboratories.	3
2.1	The configuration of Synthetic Aperture Radar. Image is taken from radartutorial.eu.	8
2.2	Geometry of spotlight mode SAR.	9
2.3	Graphical representation of phase history data.	11
2.4	Interpolation operation on phase history data.	12
2.5	Sample images of a scene at multiple DTED levels. The numbers in the images indicate the spatial resolution.	16
2.6	Configuration of SRTM. The radars used in this mission were capable of operation in X-band and C-band. Two active radar antennas were placed on the space shuttle, and two passive antennas were placed at the end of the metallic mast. Here, the metallic mast provides the spatial baseline which is needed for across-track interferometry.	18
2.7	Double slit interferometry experiment.	19
2.8	SAR Interferometry Imaging Geometry.	20

2.9	A sample raw interferogram based on ERS 1/2 data. Note the fringe pattern that continues along the range dimension (y axis). Also, fringes due to elevation can be interpreted. Image was taken from Synthetic Aperture Radar Interferometry [3].	24
2.10	Flattened interferogram example. Frequency of fringes represents the slope of the area. Image was taken from Synthetic Aperture Radar Interferometry [3].	24
3.1	Synthetic scene used in the first two experiments and the SAR images generated by the Polar Format Algorithm.	43
3.2	The results of the first experiment. The parameters λ_1^2 , λ_2^2 , and α are chosen empirically as 2, 2, and 0.000005. In the relative phase plots, true phase difference values are shown as red points, and phase differences estimated by each algorithm are shown as blue points.	45
3.3	The results of the second experiment. The parameters λ_1^2 , λ_2^2 , and α are chosen empirically as 3, 3, and 0.000005. In the relative phase plots, true phase difference values are shown as red points, and phase differences estimated by each algorithm are shown as blue points.	47
3.4	The results of the third experiment. The parameters λ_1^2 , λ_2^2 , and α are chosen empirically as 2, 2, and 0.00005. In the relative phase plots, true phase difference values are shown as red points, and phase differences estimated by each algorithm are shown as blue points.	48

3.5	The phase error estimates for Test 3. The blue solid curve represents the true phase error. The red dashed and green dash-dotted curves represent the phase error estimates obtained by SDCIA and SDA, respectively.	49
3.6	The results of the fourth experiment. The parameters λ_1^2 , λ_2^2 , and α are chosen empirically as 3, 3, and 0.00005. In the relative phase plots, true phase difference values are shown as red points, and phase differences estimated by each algorithm are shown as blue points.	50
3.7	The phase error estimates for Test 3. The blue solid curve represents the true phase error. The red dashed and green dash-dotted curves represent the phase error estimates obtained by SDCIA and SDA, respectively.	51
3.8	The results of the fifth experiment. The parameters λ_1^2 , λ_2^2 , and α are empirically chosen as 2, 2, and 0.5. In the relative phase plots, true phase difference values are shown as red points, and phase differences estimated by each algorithm are shown as blue points.	53
3.9	The results of the sixth experiment. The parameters λ_1^2 , λ_2^2 , and α are chosen empirically as 40, 40, and 0.5. In the relative phase plots, true phase difference values are shown as red points, and phase differences estimated by each algorithm are shown as blue points.	55
3.10	Phase RMSE values of SDA and SDCIA algorithms for different sparsity parameters.	56
4.1	Model of Göktürk-3 displayed at the stand of TAI during the IDEF'15.	58
4.2	Components of the SAR Interferometry Toolbox.	59

4.3	Demonstration of perpendicular baseline change with position of the scatterer. Perpendicular baseline and incidence angle change slightly with range and height.	67
4.4	Graphical User Interface of SAR Interferometry Toolbox.	69
4.5	Master image of DLR dataset.	70
4.6	A flattened interferogram example produced by the SAR Interferometry Toolbox. All processing steps except flat earth calculation for this data is performed by the SAR Interferometry Toolbox. Each cycle corresponds to 167.89 meter height change.	70
4.7	A coherence map example produced by the SAR Interferometry Toolbox.	71
4.8	A digital elevation map produced from DLR dataset. All interferometric steps are performed by SAR Interferometry Toolbox Height of ambiguity is 167.89 m/cycle.	71
4.9	Synthetic SAR Images for the Image Registration Test.	73
4.10	Mount Vesuvius Data for the the registration test. The control points are pointed out with red squares.	77
4.11	Synthetic Phase Profiles. Here, the five profiles used for 2-D phase unwrapping test operation are presented. These are pyramid, diagonal plane, sheared planes, parabolic surface, and cut pyramid. . . .	80
4.12	Standard deviation of the phase estimator given in Equation 4.6 with respect to multilooking and coherence. The image was taken from [3]	82
4.13	Synthetic Interferogram Examples.	82
4.14	A Single look interferogram and its residue map.	84

4.15	Phase RMSE's with respect to different multilooking parameters are presented. Each one of these graphs shows the RMSE in phase estimation for a different phase profile.	84
4.16	Height RMSE's with respect to different multilooking parameters for a system has height of ambiguity $h_{amb} = 100m$. Each one of these graphs are denotes the RMSE in height estimation for a different phase profile.	85
4.17	Unwrapped interferograms of pyramid. They are averaged with different multilooking windows. Clearly, we got better results with the increasing size of the multilooking window.	86
4.18	Unwrapped Interferograms of parabolic surface. They are averaged with different multilooking windows. Clearly, we got better results with the increasing size of the multilooking window.	87
4.19	Unwrapped Interferograms of diagonal plane. They are averaged with different multilooking windows. Clearly, we got better results with the increasing size of the multilooking window.	88
4.20	Unwrapped interferograms of cut pyramid plane. They are filtered with different multilooking windows.	90
4.21	Unwrapped interferograms of sheared plane. They are filtered with different multilooking windows.	91

List of Tables

2.1	DTED level specifications.	16
2.2	Tilt errors due to parallel baseline estimation errors. Baseline values are taken from the ERS-1 Toolik, Alaska mission.	28
2.3	Height errors due to parallel baseline estimation errors. Baseline values are taken from the ERS-1 Toolik, Alaska mission.	28
2.4	Height errors due to perpendicular baseline estimation errors. Base- line values are taken from the ERS-1 Toolik, Alaska mission.	28
3.1	The values of the imaging parameters used in the simulations.	42
4.1	List of the inputs required by the toolbox.	59

4.2	Registration Test Results for Synthetic SAR dataset shown in Figure 4.9. The test procedure is as follows. We assume that the user makes the specified amount of error while selecting control points in master and slave image. Suppose the user has to select two pair, it is assumed that the user makes the same amount of error while selecting both pairs. Here, we present the amount of shift between images which the registration algorithm calculated. The amount of shifts between input master and slave images in X and Y dimension are denoted by ΔX and ΔY , respectively. ΔX_{err} and ΔY_{err} represent the selection errors between the control points in master and slave images in X and Y dimensions, respectively.	75
4.3	Registration Test Results for Synthetic SAR dataset shown in Figure 4.9. The test procedure is as follows. As previous test procedure described in Figure 4.2, we assume that the user makes the specified amount of error while selecting control points in master and slave image. However, the user selects one of the pairs perfectly in this time, and makes error for the other pair. The amount of the selection error in terms of pixel are defined in the table. Here, we present the amount of shift between images which the registration algorithm calculated. The amount of shifts between input master and slave images in X and Y dimension are denoted by ΔX and ΔY , respectively. ΔX_{err1} and ΔX_{err2} are the selection errors between the first and second control pair in master and slave images in X, respectively. ΔY_{err1} and ΔY_{err2} represent the same type error for Y dimension.	76

- 4.4 Registration Test Results for the Mount Vesuvius dataset shown in Figure 4.10. The test procedure is as follows. We assume that the user makes the specified amounts of error while selecting control points in master and slave images. Suppose the user has to select two pairs of control points. It is assumed that the user makes the same amount of error while selecting both pairs. Here, we present the amount of shift between images which the registration algorithm calculated. The amounts of shift between input master and slave images in X and Y dimension are denoted by ΔX and ΔY , respectively. ΔX_{err} and ΔY_{err} represents the selection errors between the control points in master and slave images in X and Y dimensions, respectively. 78
- 4.5 Registration Test Results for Mount Vesuvius dataset shown in Figure 4.10. The test procedure is as follows. As in the previous test procedure described in Figure 4.2, we assume that the user makes the specified amount of error while selecting control points in master and slave images. However, the user selects one of the pairs perfectly this time, and makes an error for the other pair. The amount of the selection error in terms of pixels are given in the table. Here, we present the amount of shift between images which the registration algorithm calculated. The amounts of shift between input master and slave images in X and Y dimension are denoted by ΔX and ΔY , respectively. ΔX_{err1} and ΔX_{err2} are the selection errors in X between the master and slave images, in the first and the second control pairs, respectively. ΔY_{err1} and ΔY_{err2} represent the same type error in the Y dimension. 79

Chapter 1

Introduction

In this thesis we develop new tools and methods for processing interferometric synthetic aperture radar (SAR) data. The first contribution of this thesis is a sparsity-driven method for coupled interferometric SAR imaging and autofocus-ing that achieves interchannel information preservation while correcting for model errors. The second contribution of this thesis is a software toolbox for end-to-end interferometric data processing starting from image registration and ending with terrain height estimation. The purpose of this chapter is to: 1) give a quick summary of SAR and Multichannel SAR imaging; 2) underline the problems we solved; 3) introduce the solution we propose to these problems, 4) present the outline of this thesis.

1.1 Motivation

Synthetic Aperture Radar (SAR) is one of the most widely used imaging techniques in remote sensing. Due to many advantages of this imaging modality, SAR has been extensively used for military and civilian purposes. For example, the classification of military vehicles [34], the estimation of the yield of crops [26] and the detection

of earth deformations [5] are some examples of the utilization of SAR imaging systems.

In SAR imaging, a radar platform mounted on an airplane or a satellite, transmits waveforms periodically and collects the reflected signals as it moves along a trajectory. After processing the reflected signals, a 2-D image of the scene can be formed from the collected signals. Imaging quality of SAR systems is getting close to optical systems with advanced sensing and processing methodologies. SAR systems maintain well-known advantages over optical systems. For example, SAR imaging systems are capable to work during day and night under all-weather conditions. SAR systems usually work as active radar systems, so they illuminate the scene by transmitting electromagnetic waves from the radar antenna. Therefore, they do not need an illumination source to work. Plus, microwave radiation which SAR systems use can penetrate through cloud cover, haze, dust, and all but the heaviest rainfall as the longer wavelengths are not susceptible to atmospheric scattering which affects shorter optical wavelengths. In addition to these advantages, more information about the scene can be obtained with SAR compared to optical imaging, such as elevation information of the scene or under-foliage structures.

On the other hand, there are some problems and limitations of SAR imaging systems as well. Imaging of limited-extent data limits the resolution. Furthermore, common SAR processing result in causes considerable amount of sidelobes , especially when some frequencies are blocked. This problem can be addressed by with image-regularization and reconstruction algorithms. These algorithms form SAR images that are consistent with collected data. In addition, the data are regularized through a prior information term. By experience, it is demonstrated that the most common prior information is the *sparsity* of the scene in some domain.

Another common problem about SAR imaging is the autofocus problem. In radar systems, the round-trip time of the transmitted waveform, i.e., demodulation

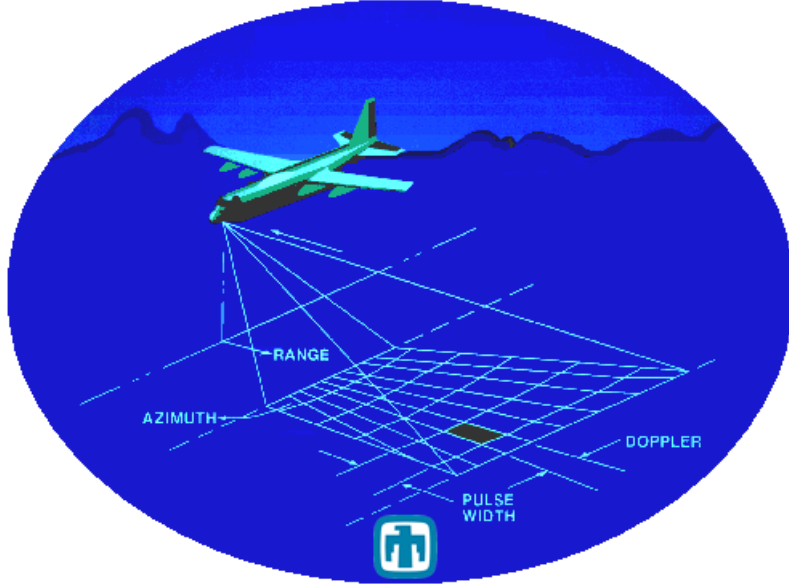


Figure 1.1: Simple illustration of SAR imaging operation. Image is taken from the web site of Sandia National Laboratories.

time, is very important for SAR image processing. Error in the demodulation time cause blurring in SAR images. This problem is called the autofocus problem in SAR literature. In SAR literature, many autofocus algorithms were proposed to solve this problem [28] [30].

Recently, Multichannel SAR imaging, such as Tomographic SAR (TomoSAR) and Interferometric SAR (IfSAR), has been of interest in SAR literature. While SAR imaging systems create a 2-D projection of the scene, the purpose of multichannel SAR imaging is to form a 3-D model of the scene. Multichannel SAR imaging modalities use two or more SAR images to create a 3-D model of the area of interest. When the images used in multichannel SAR imaging processes are formed by independent image reconstruction algorithms, the interchannel information across the image acquisitions, such as relative phase between SAR images, may degrade. This reduces the precision of the 3-D model of the scene. Therefore, there emerged a need for an image formation method which can preserve

the interchannel information between acquisitions for multichannel SAR applications. Lately, joint image reconstruction algorithms were proposed to address this issue [23] [29].

Up to this point, we have drawn attention to two problems encountered in the SAR imaging process. These are the autofocusing problem and preserving interchannel information between SAR images. In the literature, there are different solutions to each of the problems we posed. On the other hand, there is the deficiency of an algorithm which can solve the autofocusing problem and preserving interchannel information for multichannel SAR imaging modalities at the same time. This constitutes the main motivation for our work.

The main objective of this work is to develop an imaging algorithm to solve autofocusing problem of SAR imaging and to preserve interchannel information between SAR acquisitions at the same time. Besides that it is aimed to produce a SAR Interferometry Toolbox which is capable to produce 3-D height maps from SAR images within the content of the project supported by ASELSAN.

1.2 Contribution of the Thesis

Instead of solving the problems we have described in the previous section independently, we propose a sparsity-driven method for coupled image formation and autofocusing (SDCIA) based on multi-channel data collected in interferometric synthetic aperture radar (IfSAR). SDCIA is a joint image reconstruction and regularization algorithm. Basically, the combination of SDA by Önhon and Çetin [20] and Joint Enhancement by Dual Descent by Ramakrishnan and Ertin [23] constitutes SDCIA.

Our coupled optimization formulation involves a sparsity enforcing penalty term for each image. In addition to that, it contains a term penalizing differences

of reflectivity magnitudes at pairs of pixels in the IfSAR images as well. The image acquisitions for IfSAR are done in a close formation, so the supports of these signals are expected to be same. The phase as an explicit variable of optimization in the observation matrix is updated to eliminate phase errors caused by demodulation time uncertainties.

SDCIA solves this coupled optimization problem iteratively. Each iteration has two major steps. In the first step, a Lagrangian method is used to optimize the cost function with respect to image fields, as described in [23]. Then, the cost function is optimized with respect to the phases, as in [20]. In order to demonstrate the effectiveness of our method, SDCIA has been tested in different scenarios, and the results of the simulations are presented.

In addition, SAR Interferometry Toolbox was created within the master project financed by ASELSAN, one of the leading defence companies in Turkey. The toolbox is capable to perform the major steps of SAR Interferometry processing, from registration to height map generation.

1.3 Organization of the Thesis

This thesis is organized as follows. In Chapter 2, preliminary information is given to provide a basis for the rest of the thesis. Three different subjects are summarized in Chapter 2. First, the fundamentals and mathematical description of spotlight mode of SAR is presented, since spotlight mode of SAR is our main focus among SAR imaging modalities due to the reasons given in the next chapter. Then, principles and applications of Interferometric SAR are explained. As we mentioned earlier, Interferometric SAR is a multichannel SAR imaging modality. As distinction from SAR, the purpose of IfSAR is to create 3-D models of the scene. In Chapter 2, a brief summary of Interferometric SAR literature and mathematical

foundations of this imaging modality are introduced. Lastly, regularization-based SAR imaging is discussed in this chapter.

The proposed method, Sparsity-driven for Coupled Imaging and Autofocusing, is introduced in Chapter 3. SDCIA has been tested for different cases in order to show its effectiveness. The results are presented in this chapter as well.

The fourth chapter is a summary of the project we carried out in collaboration with ASELSAN, one of the biggest defence companies in the Turkey. In addition to my research studies, I worked on a project, SAR Interferometry Algorithm Development Project, sponsored by ASELSAN. The main objective of this project was to produce a software toolbox which can process IfSAR data. In this chapter, a brief summary of the work we have done for this project and the outcomes of the project are presented. Finally, potential future directions and comments are discussed in Chapter 5.

Chapter 2

Preliminaries

The purpose of this chapter is to present the necessary background information to understand the research we have done and the SAR Interferometry Toolbox Project. Within this context, SAR imaging, SAR Interferometry and regularization based image reconstruction are briefly summarized in this chapter.

2.1 Synthetic Aperture Radar

Synthetic Aperture Radar (SAR) is a radar technique used to obtain a 2-D projection of the scene. Radar systems work based on the principle of measuring the round trip travel time of the transmitted electromagnetic waveform. Therefore, the distance between the radar antenna and the objects can be estimated from the reflected waveforms. However, the reflected waveforms provide only one dimensional information about the position of the objects, radial distance between radar antenna and objects.

Synthetic Aperture Radar is a radar imaging technique to solve the cross-range resolution problem. An example configuration for SAR is demonstrated in Figure 2.1. In this technique, the radar antenna is mounted on a mobile platform, for

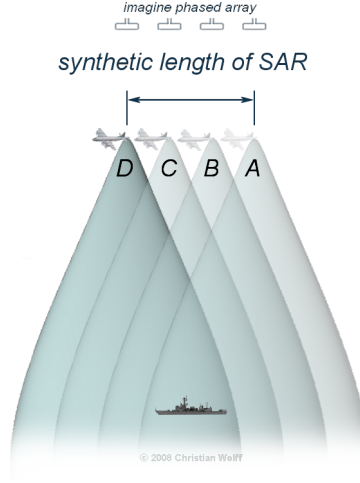


Figure 2.1: The configuration of Synthetic Aperture Radar. Image is taken from radartutorial.eu.

example an airplane or a satellite. As this platform moves along its trajectory, the scene is illuminated with electromagnetic waveforms periodically, and the reflected waveforms are collected as well. Basically, a large synthetic aperture is created to get a resolution in cross-range dimension. After collection of reflected waveforms from the scene, a 2-D projection of the scene can be formed by using image formation algorithms.

There are several SAR data collection modes. In this thesis, we provide a brief overview of a widely used monostatic mode of SAR, namely spotlight mode of SAR. For the sake of brevity, we do not discuss other modes including bistatic modes of SAR [17], ScanSAR [2], and Hybrid SAR [4].

2.1.1 Spotlight SAR Imaging Model

Spotlight mode SAR involves observing only a specific area on the ground by rotating the radar antenna to aim at that area through the flight path, as illustrated in Figure 2.2. By observing the scene from a larger range of azimuth angles,

spotlight mode SAR achieves high cross-range resolution [13]. The cross-range resolution in spotlight mode SAR is usually higher than Stripmap mode of SAR with a similar flight path, with the tradeoff of smaller area coverage [3].

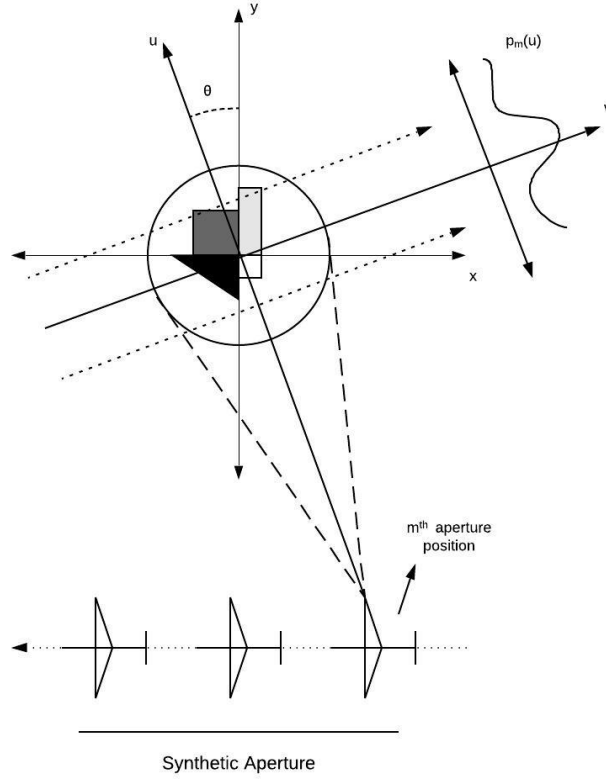


Figure 2.2: Geometry of spotlight mode SAR.

Majority of SAR systems illuminate the scene with a chirp signal defined as follows:

$$s(t) = \Re(\exp(j(\omega_0 t + \alpha t^2))) \quad (2.1)$$

where ω_0 , 2α are the center frequency of the transmitted chirp signal and the chirp rate of the signal, respectively. In spotlight-mode SAR, the relationship between

the transmitted signal and the reflected signal at observation angle θ_m after several pre-processing steps is given by [8]:

$$Z(U) = \bar{r}_m(t) = \int_{|u| \leq L^2} p_m(u) e^{-jUu} du \quad (2.2)$$

where $p_m(u)$ is the projection of the field at the m^{th} aperture position:

$$p_m(u) = \iint_{x^2+y^2 \leq L^2} \delta(u - x \cos \theta - y \sin \theta) F(x, y) dx dy \quad (2.3)$$

Here, $F(x, y)$ denotes the reflectivity field, L is the scene radius, and τ_0 is the demodulation time of the transmitted signal and c is the speed of light. The spatial frequency U is given by:

$$U = \frac{2}{c}(\omega_0 + 2\alpha(t - \tau_0)). \quad (2.4)$$

The reflected signal at the m^{th} platform position, i.e., $\bar{r}_m(t)$, corresponds to a spatial Fourier transform. After collecting the reflected signals from all platform positions and sampling those reflected signals in time, we get a sampled 2-D spatial Fourier transform of the scene, also called the phase history data. In Figure 2.3, an illustration of the support of the phase history data of Spotlight mode of SAR is presented.

When the reflected signal is discretized, the observation kernel and the unknown scene can be approximated as a matrix and a vector, respectively. Then, the SAR observation process can be modeled as a matrix-vector product as shown in Eqns. (2.5) and (2.6).

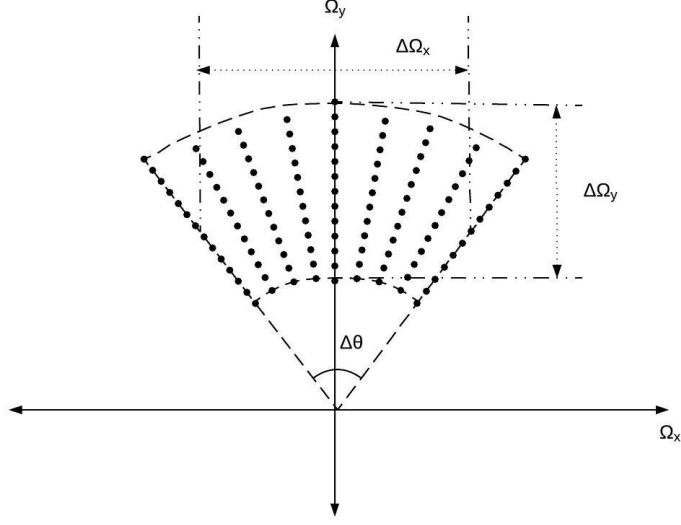


Figure 2.3: Graphical representation of phase history data.

$$\begin{bmatrix} \bar{g}_1 \\ \bar{g}_2 \\ \vdots \\ \bar{g}_M \end{bmatrix} = \begin{bmatrix} \bar{C}_1 \\ \bar{C}_2 \\ \vdots \\ \bar{C}_M \end{bmatrix} f + v \quad (2.5)$$

$$g = Cf + v \quad (2.6)$$

where \bar{r}_m and \bar{C}_m denote the reflected signal and the discretized observation kernel, respectively, at the m^{th} position of the radar platform, f is an $N \times 1$ column vector representing the discretized scene, and v denotes measurement noise. Eqn. 2.6 is the overall observation model where g denotes the entire phase history data and C is the overall observation matrix. A detailed explanation of this formulation can be found in [8]. Given this observation model, image reconstruction algorithms can be used for forming images from the collected SAR data.

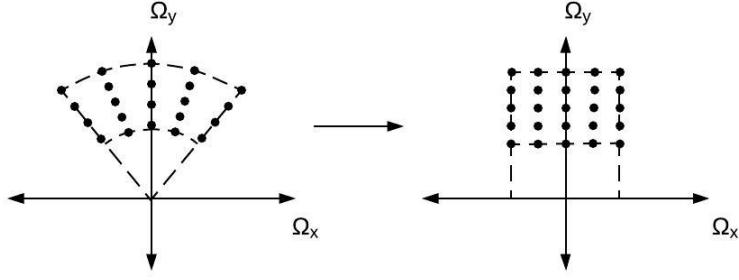


Figure 2.4: Interpolation operation on phase history data.

2.1.2 Conventional Image Formation Algorithms

Polar Format Algorithm

Polar Format Algorithm (PFA) is one of the widely used SAR image formation algorithms.

In Section 2.1.1, it was stated that collected SAR data corresponds to a 2-D bandpass Fourier transform of the scene. This is called phase history data, and it is depicted in Figure 2.3 as an annulus. PFA forms SAR images in the following way. First, PFA interpolates the data from a polar grid to a Cartesian grid as shown in Figure 2.4. Then, a 2-D inverse Fourier transform is applied to the interpolated data to get 2-D SAR images.

2.1.3 SAR Autofocus Problem

Autofocusing is one of the important problems in SAR imaging systems. In SAR imaging, one of the processing steps is the demodulation of the collected waveforms. To do this operation, the demodulation time of transmitted waveform should be known precisely. Theoretically, demodulation time is calculated as follows.

$$\tau_0 = \frac{2d_0}{c} \quad (2.7)$$

where d_0 is the distance between platform and scene center. Basically, demodulation time is the round trip travel time of the transmitted waveform.

Conventionally, d_0 is calculated by hardware systems on the SAR platforms, called as inertial measurement units (IMU's). However, it is very difficult to estimate d_0 with the required precision by high quality IMU's. This would eventually lead to errors in demodulation time. As a result, any error in demodulation time would show its effect as phase errors in demodulated data. To solve this problem, many post-processing algorithms were proposed, and they are called autofocus algorithms.

Autofocusing algorithms can alleviate phase error problems related to the limited accuracy of IMUs, as well as related to other factors. Precision of IMU's can only decrease the phase errors due to position uncertainties of the imaging platform. On the other hand, there are other factors which can cause phase errors in the data. Weather conditions and Faraday rotation are some examples to these. Autofocusing algorithms can handle all phase error types without discriminating.

The model we established in Section 2.1.1 is based on the assumption that all system parameters are known precisely. If demodulation time is not known precisely, there will be an error term in delayed in-phase and quadrature versions of the transmitted chirp signal as shown in Equation (2.8) and (2.9).

$$\cos(w(t - \tau_0 + \epsilon) + \alpha(t - \tau_0 + \epsilon)^2) \quad (2.8)$$

$$- \sin(w(t - \tau_0 + \epsilon) + \alpha(t - \tau_0 + \epsilon)^2) \quad (2.9)$$

where ϵ stands for demodulation time error. Therefore, we would get extra error

terms in the output of the preprocessed SAR data.

$$Z_\epsilon(U) = \bar{r}_{m_\epsilon}(t) = e^{-j\epsilon^2\alpha} e^{j\frac{\epsilon c}{2}U} \int_{|u| \leq L} p_m(u) e^{-jUu} du \quad (2.10)$$

According to Equation (2.2), a relationship between the phase corrupted data and error-free data can be established as follows.

$$Z_\epsilon(U) = e^{-j\epsilon^2\alpha} e^{j\frac{\epsilon c}{2}U} Z(U) \quad (2.11)$$

Since $\epsilon^2\alpha \ll 1$, $e^{-j\epsilon^2\alpha}$ can be approximated as 1. Then, the relationship becomes:

$$Z_\epsilon(U) = e^{j\frac{\epsilon c}{2}U} Z(U) \quad (2.12)$$

If we replace U in Equation (2.12) with Equation (2.4), then we get

$$Z_\epsilon(U) = e^{j\epsilon w_0} e^{j\epsilon(2\alpha(t-\tau_0))} Z(U) \quad (2.13)$$

Usually, the term $2\alpha(t - \tau_0)$ is much smaller than w_0 . Therefore, $e^{j\epsilon(2\alpha)(t-\tau_0)}$ can be neglected. Then, we obtain

$$\begin{aligned} Z_\epsilon(U) &= e^{j\epsilon w_0} Z(U) \\ Z_\epsilon(U) &= e^{j\phi} Z(U) \end{aligned}$$

where ϕ is the phase error in the data due to demodulation time error. Such phase errors cause blurring in the cross-range direction [13]. Techniques designed to alleviate this effect are called autofocus algorithms. Previously, many autofocusing algorithms were proposed to solve this problem. Phase-Gradient Autofocus (PGA) [28] and Multi-Channel Autofocus (MCA) [18] are some examples to these algorithms.

Recently, a regularization based algorithm, Sparsity-Driven Autofocus, was proposed by Önhon and Çetin [20]. This method eliminates the autofocus problem by solving the following optimization problem with respect to both the field vector and observation matrix during the image formation process:

$$\hat{f}, \hat{\phi} = \underset{f, \phi}{\operatorname{argmin}} \|g - C(\phi)f\|_2^2 + \lambda^2 \|f\|_p^p \quad (2.14)$$

2.2 SAR Interferometry

In this section, we focus on a particular SAR imaging modality, namely Interferometric Synthetic Aperture Radar (IfSAR). We provide a coverage of basics of IfSAR, discuss important technical aspects, and provide pointers to fundamental and recent literature on the topic.

It is possible to get 2D interpretation of surfaces with basic SAR systems. Interferometric SAR aims to go beyond that capability to provide 3D information. To create a digital elevation map, a 3D model of the observation area, by using phase information is the main idea in IfSAR. In the following sections, we describe the benefits and main stages of, as well as different approaches for IfSAR sensing and processing.

2.2.1 Image Resolution Quality Measurements

To determine the quality of an IfSAR observation, there is a quality reference system called Digital Terrain Elevation Data (DTED). By using this system, we can classify images in terms of their resolution.

DTED classification system has 6 quality measurement levels, from 0 to 5, three of them are shown in Table 2.1. For instance, DTED level 1 implies that pixels have 3 second post spacing, nominally 100 m [1]. The higher levels, such

	Spatial Resolution	Absolute Vertical Accuracy	Relative Vertical Accuracy	Absolute Circular Geolocation Accuracy	Relative Circular Geolocation Accuracy
<i>DTED-I</i>	90m x 90m	>30m	>20m	>50m	-
<i>DTED-II</i>	30m x 30m	>18m	>12m	>23m	>15m
<i>HRTI-III</i>	12m x 12m	>10m	>2m	>3m	>10m

Table 2.1: DTED level specifications.

as DTED level 5, correspond to higher resolutions. A system should reach 0.037 sec resolution, nominally around 1 meter, to satisfy the DTED level 5 criterion. Figure 2.5 contains images of a particular scene obtained at different DTED levels.

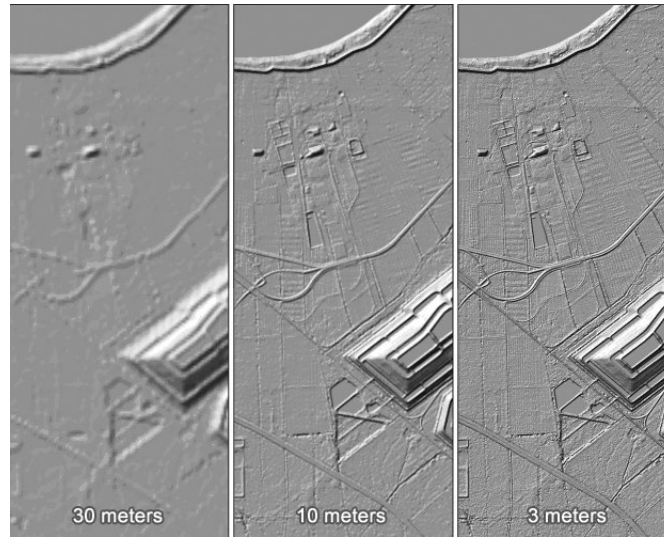


Figure 2.5: Sample images of a scene at multiple DTED levels. The numbers in the images indicate the spatial resolution.

2.2.2 Examples of Operational IfSAR Satellite Systems

RADARSAT (Canada)

RADARSAT is a pair of remote sensing satellites. The first one, RADARSAT-1, was launched in 1995, and the second one, RADARSAT-2, was launched in 2007.

This system operates in the C-band [10]. It has the capability to perform tandem interferometric imaging missions.

Shuttle Radar Topography Mission (USA)

Shuttle Radar Topography Mission (SRTM) is a SAR Interferometry mission which is carried by the Jet Propulsion Laboratory, NASA. For 11 days in February 2000, SRTM successfully recorded IfSAR data. The data acquired in C band and X band have been processed into the first global digital elevation models at 1 arc sec resolution [22]. This corresponds $30\text{ m} \times 30\text{ m}$ resolution at the equator. What distinguishes SRTM from previous interferometric systems is that it is capable of performing one pass interferometry instead of repeat pass interferometry. This became possible with specific design of the space shuttle used in this mission as seen in Figure 2.6. Thus, it minimizes the adverse effects of temporal decorrelation and dynamic atmospheric events, and also minimizes height errors due to baseline measurement errors.

ERS, Envisat, TerraSAR-X (Europe)

The field of satellite-based SAR and IfSAR systems is very active in Europe with many research groups, particularly in Italy and Germany. In this section, brief information will be provided on their major projects.

ERS 1 and ERS 2 are satellites designed and produced by the European Space Agency [10]. Just like RADARSAT pairs, they are capable of carrying out tandem interferometric operations. ERS 1 was launched in 1991. Then, ERS 2 was launched in 1995 in order to carry out interferometric SAR operations. One important novel aspect of this satellite pair is that their orbits are phased to orbit the Earth 24 hours apart [10]. This was quite a short time for this type of operation, and this short interval provides a good coherence between collections. This increases the

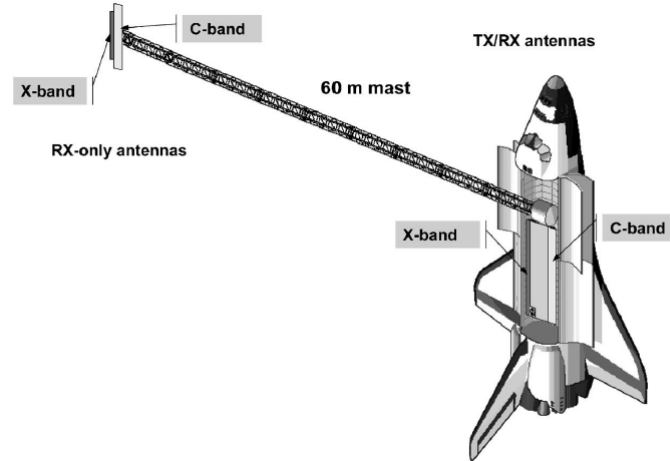


Figure 2.6: Configuration of SRTM. The radars used in this mission were capable of operation in X-band and C-band. Two active radar antennas were placed on the space shuttle, and two passive antennas were placed at the end of the metallic mast. Here, the metallic mast provides the spatial baseline which is needed for across-track interferometry.

quality of the resulting interferograms.

Envisat was launched in 2002. This satellite was more comprehensive than ERS 1 and ERS 2. It was carrying several optical and radar instruments [10]. Its largest sensor was an advanced synthetic aperture radar operating at C-band. The main aim of Envisat was to perform more advanced remote sensing missions, such as ocean observation or ice observation. ENVISAT was able to collect important data for analyzing climate change.

TerraSAR-X is an earth observation satellite launched in 2007 and operated by the German Aerospace Agency, DLR [17] [3]. Its twin satellite TanDEM-X was launched in 2010. TanDEM-X is identical to TerraSAR-X, aimed for operating interferometric operations.

2.2.3 Principles of Interferometry

IfSAR involves a combination of SAR imaging and the principle of interferometry. Synthetic aperture radar is a coherent imaging method and generates a complex-valued image which involves the magnitude and the phase of the reflectivity at each point in the scene. What we display and use as a conventional SAR image uses the magnitudes and not the phases. This motivates the question of how reflectivity phase can be used to extract further information about the scene.

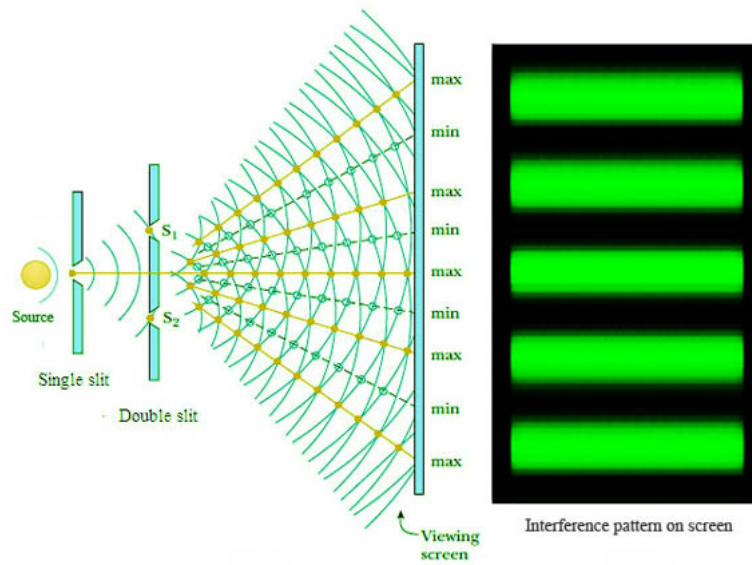


Figure 2.7: Double slit interferometry experiment.

The principle of a basic two slit interferometry experiment is illustrated in Figure 2.7. Interferometry involves two wave sources, and we can calculate the phase difference between the corresponding waves based on the position of the glitches on the screen.

Interferometric SAR is the combination of SAR imaging and interferometry. IfSAR uses the relative phase between scene reflectivities corresponding to two data collections as an additional information source about the scene. As we describe in the following sections, this can provide information about elevation at each point

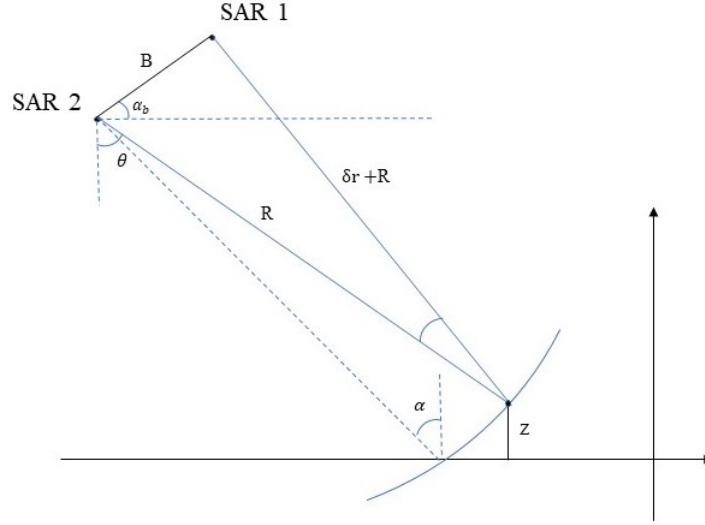


Figure 2.8: SAR Interferometry Imaging Geometry.

in the scene.

2.2.4 Fundamentals of SAR Interferometry

In this section, basic mathematical derivations about IfSAR phase difference calculations will be given. SAR Interferometry imaging geometry is presented in Figure 2.8. More detailed derivations can be found in [10].

Phase and Height Relationship

SAR Interferometry makes use of the relative phase between the first and the second SAR acquisition to estimate the height of the scene. The relationship between phase and height is defined with height sensitivity.

In order to establish a relationship between phase and height, we would start with expressing height of the scene by system parameters. From Figure 2.8, the

height of the scene can be expressed as follows:

$$z = r \cos \alpha - r \cos \theta \quad (2.15)$$

where α and θ are defined in Figure 2.8.

This result can be found by using geometric identities. In order to establish a relationship between phase and height, we would continue with calculating range difference between the acquisitions. As it is shown in Figure 2.8, a small range difference between image acquisitions is expected due to their position differences. This range difference, δr , can be calculated by Equation (2.16).

$$\delta r = -b \sin(\theta - \alpha_b) \quad (2.16)$$

Usually, the distance between platforms, i.e. baseline, is relatively too small compare to slant range. Therefore, $\Delta\theta$, incidence angle difference between acquisitions, is expected to be very small.

As shown in Figure 2.8, any change in the position of the scatterer in range or elevation dimension would change the geometry of the acquisition. This would change range difference between image acquisitions as well. Geometrically, it is easy to see a change in the position of the scatterer in z dimension would create a change in range difference. Mathematically, this relation can be formulated as the ratio of their partial derivatives with respect to θ as follows:

$$\frac{\partial \delta r}{\partial z} = \frac{\frac{\partial \delta r}{\partial \theta}}{\frac{\partial z}{\partial \theta}} \quad (2.17)$$

These partial derivatives are given as follows:

$$\partial\delta r = -b \cos(\theta - \alpha_b) \quad (2.18)$$

$$\partial z = R \sin(\theta) \quad (2.19)$$

The ratio of the derivatives of z and δr constitutes the relationship between range difference between acquisitions and the height of the scene.

$$\frac{\partial\delta r}{\partial z} = -\frac{b \cos(\theta - \alpha)}{r \sin \theta} = -\frac{b_{\perp}}{r \sin \theta} \quad (2.20)$$

The effect of any difference in slant range distances of the image acquisitions is a phase shift in transmitted waveforms. The amount of phase shifts due to range difference is determined as shown in Equation (2.21). Here, the round trip distance of the transmitted waveform is taken into account. Therefore, this formula gives the amount of phase shifts due to $2\delta r$ slant range difference.

$$\delta r = -\frac{\lambda}{4\pi} \psi \quad (2.21)$$

Then, δr term in Equation 2.20 is replaced with Equation 2.21.

$$\frac{\partial\psi}{\partial z} = \frac{4\pi}{\lambda} \frac{B_{\perp}}{R \sin \theta} \quad (2.22)$$

The relationship we found is called height sensitivity in SAR Interferometry literature. The amount of phase shift between first and second SAR images due to any height change in the scene is determined with this relation.

Relative Phase Calculation

Relative phase differences between SAR images can be obtained by multiplying the first, or master, SAR image with the complex conjugate of the second, or slave, image (or vice versa):

$$\varphi_{ML} = \angle \left(\sum_{n=1}^N u_1^* u_2 \right) \quad (2.23)$$

Since phase exhibits statistical behaviour, this multiplication yields only a maximum likelihood (ML) estimation of the phase difference between two SAR images [25]. In order to increase the precision of this estimate, an averaging operation can be performed. In the SAR interferometry literature, this is often called complex multilooking. Basically, the precision of the phase estimate increases with the size of the window used in multilooking. The number of pixels used in multilooking can be increased insofar as the resolution criterion permits.

Interferogram Flattening

The phase difference between two interferometric SAR image pairs has two main geometric contributions. These are range and elevation. In other words, the phase difference between observations depends on the range values as well. Therefore, we observe a fringe pattern in the range direction that has nothing to do with elevation. A sample interferogram that exhibits such fringes in the range direction is shown in Figure 2.9.

In order to obtain height information, fringes caused by range should be eliminated. This operation is called interferogram flattening. After this operation, fringe patterns become a direct indicator of height change in the scene. The flattened version of the interferogram in Figure 2.9 is shown in Figure 2.10.

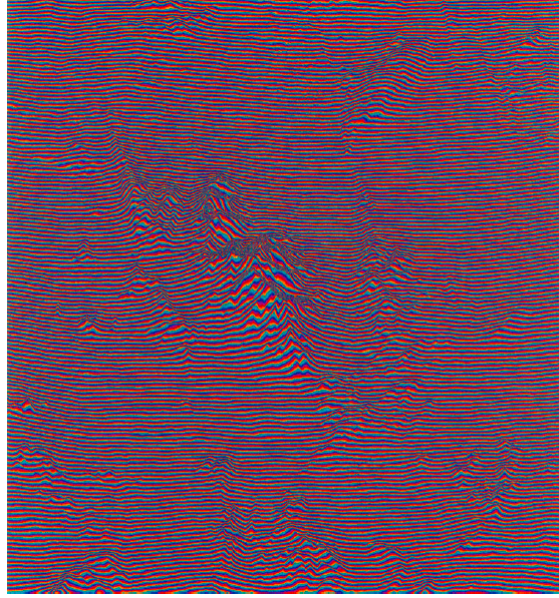


Figure 2.9: A sample raw interferogram based on ERS 1/2 data. Note the fringe pattern that continues along the range dimension (y axis). Also, fringes due to elevation can be interpreted. Image was taken from Synthetic Aperture Radar Interferometry [3].

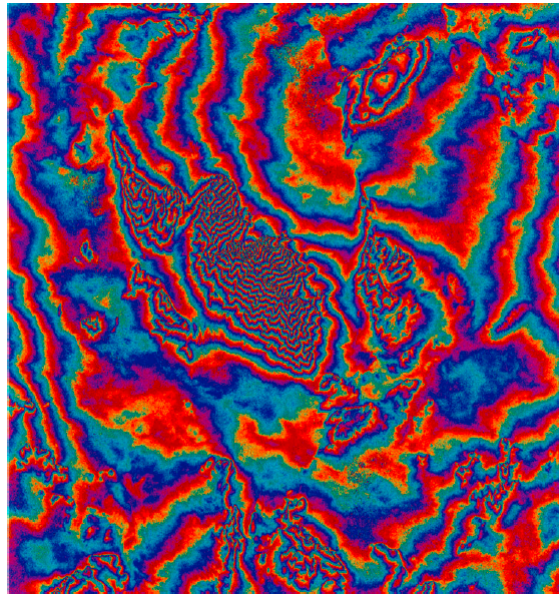


Figure 2.10: Flattened interferogram example. Frequency of fringes represents the slope of the area. Image was taken from Synthetic Aperture Radar Interferometry [3].

2-D Phase Unwrapping

Since unwrapped phase is the key for revealing height information, the accuracy of this step has crucial importance for the SAR Interferometry process. As shown in Figure 2.10, only the principal value of phase, i.e., wrapped phase, can be observed due to its periodic nature. In order to reach the height information of the scene, the real phase value should be found via 2-D phase unwrapping algorithms.

$$\psi_{real} = \psi_{wrapped} + 2\pi n \quad n \in \mathbb{Z} \quad (2.24)$$

The phase unwrapping process involves algorithms for converting the wrapped phase estimate to the actual unwrapped phase estimate. Although this seems like a straightforward operation, 2-D phase unwrapping is a hard engineering problem.

Although there exists effective and efficient algorithms for phase unwrapping, we cannot say it is a standardized process at this point. Consequently, it is still an active research area. If we assume that there is no phase discontinuity, called residues [3], the phase unwrapping problem becomes much easier. Nevertheless, this is usually not satisfied in real data, because of phase shifts due to sharp elevation changes. There are a large number of phase unwrapping algorithms, including, e.g. Unweighted Least Mean Squares method [12] and the Minimum Cost Flow method [9].

2.2.5 SAR Interferometry Baseline Problem

Several factors can impact height accuracy of SAR Interferometry systems. However, orbit determination, in particular baseline estimation, is the dominant error source among systematic errors according to [10]. Baseline estimation is a particularly important problem for repeat-pass IfSAR, because any error in the estimated baseline may result in much higher height errors than errors due to other param-

ter imperfections. Just as an example, the same numerical error in the position of the platform would constitute a much larger percentage error on the baseline than say on the altitude of the platform. Usually, altitudes of space-borne SAR systems are on the order of kilometers. Any deviation from this value would be negligible unless this deviation is on the order of 10 or 100 meters. Fortunately, altitude precision of the current systems is far better. On the other hand, baselines are on the order of few hundred meters. As a consequence, baseline errors would have a higher impact on height accuracy.

Height errors due to baseline estimation consists of two component, the error due to ΔB_{\perp} , the perpendicular component of baseline, and that due to ΔB_{\parallel} , the component of the baseline parallel to range. There are different consequences of these two types of baseline estimation errors. ΔB_{\perp} causes a bias in height estimation. The derivation of height errors due to perpendicular baseline errors is provided below.

Let $\Delta\psi_{total}$ denote the total phase difference. Then we have:

$$\Delta\psi_{total} = \frac{4\pi}{\lambda} \frac{B_{\perp} + \Delta B_{\perp}}{R \sin(\theta_i)} \quad (2.25)$$

where B_{\perp} is the nominal baseline and ΔB_{\perp} is the perpendicular baseline error. Accordingly, the phase difference caused by the perpendicular baseline error is given by:

$$\Delta\psi = \frac{4\pi}{\lambda} \frac{\Delta B_{\perp}}{R \sin(\theta_i)} \quad (2.26)$$

If we convert this phase error to height error by using Equation 2.22, we obtain:

$$\Delta h = h \frac{\Delta B_{\perp}}{B_{\perp}} \quad (2.27)$$

which says height errors due to perpendicular baseline errors only depend on to-

pographic height and the ratio of B_{\perp} error and B_{\perp} .

Similarly, parallel baseline error causes some height errors in DEM. Height error due to ΔB_{\parallel} is given by [14]:

$$\Delta h = r \sin(\theta_i) \frac{\Delta B_{\parallel}}{B_{\perp}} \quad (2.28)$$

where h , r , θ_i and B_{\perp} are topographic height, range, incidence angle, and perpendicular baseline, respectively. A parallel baseline error will furthermore cause a tilt of the DEM which is given by [14]:

$$\psi_{tilt} = \frac{\Delta B_{\parallel}}{B_{\perp}} \quad (2.29)$$

Baseline determination is a very important problem for interferometric SAR missions. In TanDEM-X, 1-2 mm platform position accuracy was achieved [15] [14]. On the other hand, the systems used in ERS-1 were not able to achieve this level accuracy. Baseline estimates were accurate to within 30 cm. Thus, a calibration process was adopted by determining tie points in the scene in order to alleviate height errors due to baseline errors [31]. In addition, by using GPS points on the earth instead of random tie points, it was possible to decrease height estimation errors due to baseline variations to 5 m rms value when decorrelation was small. This was sufficient for DTED-II level performance. Also, some alternative baseline estimation techniques are presented in [27], such as measuring fringe frequency in flat areas. Novel satellite systems have shown that better position accuracy is possible without using these types of techniques. In Tables 2.2 , 2.3, and 2.4, a baseline error analysis for the ERS-1 interferometric mission is presented.

Normal Baseline	Tilt Errors		
	ΔB_{\parallel} (1mm)	ΔB_{\parallel} (10mm)	ΔB_{\parallel} (10cm)
	$\Delta h/\Delta s$ (tilt)	$\Delta h/\Delta s$ (tilt)	$\Delta h/\Delta s$ (tilt)
40.4m	2.47cm/km	24.75cm/km	2.47m/km
201.2m	0.49cm/km	4.97cm/km	49.7cm/km

Table 2.2: Tilt errors due to parallel baseline estimation errors. Baseline values are taken from the ERS-1 Toolik, Alaska mission.

Normal Baseline	Height Errors		
	ΔB_{\parallel} (1mm)	ΔB_{\parallel} (10mm)	ΔB_{\parallel} (10cm)
	Δh	Δh	Δh
40.4m	7.95m	79.5m	795m
201.2m	1.597m	15.97m	159.7m

Table 2.3: Height errors due to parallel baseline estimation errors. Baseline values are taken from the ERS-1 Toolik, Alaska mission.

Normal Baseline	Height Errors			
	ΔB_{\perp} (1cm)	ΔB_{\perp} (1cm)	ΔB_{\perp} (10cm)	ΔB_{\perp} (10cm)
	$\Delta h(h = 9km)$	$\Delta h(h = 4.5km)$	$\Delta h(h = 9km)$	$\Delta h(h = 4.5km)$
40.4m	2.22m	1.11m	22.2m	11.2m
201.2m	0.44m	0.22m	4.4m	2.2m

Table 2.4: Height errors due to perpendicular baseline estimation errors. Baseline values are taken from the ERS-1 Toolik, Alaska mission.

2.3 Regularization Based Image Reconstruction

Previously we talked about the polar format algorithm as a conventional SAR image formation approach. More modern approaches to the SAR image reconstruction problem include regularization-based methods. Such methods have been used to solve inverse problems in a variety of applications. Here we focus on regularization-based SAR imaging, built on a discretized observation model as we describe below. In that sense, this type of approaches can be applied to many engineering problems. An observation system in discrete form can be formulated as follows.

$$g = Cf + n \quad (2.30)$$

where C , g , f , and n are the observation kernel based on the system parameters, the collected data vector from indirect observations, the unknown reflectivity field and measurement noise, respectively. As an easy solution, an estimate of the field vector, \hat{f} , can found by multiplying g vector with the inverse of the observation matrix C . However, this solution may not be feasible always. Basically, there are 4 problems which we have to handle to use this type approach.

First, due to the observation noise, there may not exist any f which solves this equation exactly. Second, if the null-space of C is nonempty which means that there are not as many independent observations as unknowns, then the solution is not unique. Third, there is a stability problem. The estimate of f is desired to remain stable in the presence of perturbations in the observations. The fourth issue is that the need to incorporate any prior knowledge of f to the solution [7].

In order to overcome these problems, different solution methods were used, such as Least Squares Solution or Tikhonov Regularization.

2.3.1 Non-Quadratic Regularization

Non-Quadratic Regularization is one of the image regularization and reconstruction methods. Mathematical formulation of a particular non-quadratic regularization method is given below.

$$\hat{f} = \underset{f}{\operatorname{argmin}} \|g - Cf\|_2^2 + \lambda^2 \|f\|_p^p \quad (2.31)$$

It incorporates prior information about the scene f through a term added to the original least squares cost function. Here, the first term ensures the consistency of the solution with the observed data. The second term is called a side constraint. The prior information about the field is imposed by this term. The effect of this term is adjusted by the regularization parameter λ .

While some engineering problems needs smooth solutions, sparse solutions, i.e., solutions in which there are only few non-zero pixels in the field vector, may fit better in some engineering applications, such as radar imaging. In this case, a great energy concentration is needed. Studies showed that non-quadratic regularization shows greater energy concentration then Tikhonov regularization. As the side constraint, a variety of terms with different regularization functionals can be selected. One of them is the general family of ℓ_p -norm constraints, as show in Equation (2.32).

$$\|f\|_p^p = \left(\sum_{i=1}^N |f_i|^p \right) \quad (2.32)$$

In spectral analysis, ℓ_p -norm constraints, where $p < 2$, have been shown to result in higher resolution spectral estimates compared to the ℓ_2 -norm case. Moreover, smaller value of p implies less penalty on large pixel values as compared to larger p . Based on these observations, ℓ_p -norm constraints with $p < 2$ are good choices to obtain sparse solutions.

2.3.2 Joint Enhancement Problem in IfSAR

Relative phase between SAR images contains valuable information. As we mentioned in earlier sections, it can be used to estimate the height of the scene in SAR interferometry. However, this relative phase could be degraded when independent enhancement methods, such as Tikhonov or Non-quadratic regularization, are used over SAR image pairs to enhance their resolutions [23].

For preservation of the inter-channel information in IfSAR, several joint image enhancement algorithms were proposed. Some of them are listed below.

Existing Solutions to the Joint Enhancement Problem

Joint Enhancement by Dual Descent Previously, Ramakrishnan et al. introduced Joint Enhancement by Dual Descent Method [23], a joint image enhancement method with a pixel-level equality constraint on reflectivity magnitudes of IfSAR image pairs. This image reconstruction algorithm enables the use of inter-channel information with this constraint while using sparsity penalties on each image. However, this technique does not provide a solution to the autofocus problem. Mathematical formulation of this technique is given as follows.

$$\min_{f_1, f_2, \phi_1, \phi_2} L(f_1, f_2) \quad (2.33)$$

where

$$\begin{aligned} L(f_1, f_2) &= \|g_1 - C_1 f_1\|_2^2 + \|g_2 - C_2 f_2\|_2^2 + \lambda_1^2 \|f_1\|_1^1 + \lambda_2^2 \|f_2\|_1^1 \\ \text{subject to } & |(f_1)_i| = |(f_2)_i| \quad i = (1 \dots N) \end{aligned}$$

Iterative Hard Thresholding Another algorithm, joint image enhancement by iterative thresholding [19], was proposed by Muirgrew et al. In this approach,

the enhancement problem over interferometric images is solved by iterative hard thresholding [6] and the autofocus problem is solved by an observation matrix update. The field vector update of this method is given below.

$$f_{s,m}^{n+1} = H_{\Gamma^n}(f_{s,m}^n + \mu C_m^H(g_{s,m}\Psi(\psi_m)C_m X_{s,m}^n)) \quad (2.34)$$

where $f_{s,m}$, $g_{s,m}$, C_m are the field vector, the data vector and the observation matrix for the m^{th} acquisition.

Complex Approximate Message Passing Different solution is ℓ_1 regularization via complex approximate message passing algorithm [29]. This algorithm solves a joint optimization problem with a joint sparsity penalty term by using complex approximate message passing.

Chapter 3

Sparsity-driven Coupled Imaging and Autofocusing for Interferometric SAR

The purpose of this chapter is to introduce the joint image enhancement method, Sparsity-driven Coupled Imaging and Autofocusing (SDCIA) for Interferometric SAR. In this chapter, we explain the fundamentals of our method, SDCIA, and present the results of our experiments evaluating this method.

3.1 Introduction

Synthetic Aperture Radar (SAR) is a widely used imaging technique in remote sensing. In SAR imaging, a radar platform mounted on an airplane or a satellite, transmits waveforms periodically and collects the reflected signals as it moves along a trajectory. After processing the reflected signals, a 2-D image of the scene can be formed from the collected signals. As in other imaging modalities, there are many factors that can degrade the performance of SAR systems. One such

factor affecting the performance of SAR imaging systems is platform location uncertainties. Any error in the location of the imaging platform during SAR imaging causes an error in the demodulation time of the reflected echo, leading to phase errors in the collected data. The effect of such phase errors appears as defocusing in the formed imagery. These motion errors do not only degrade the resolvability of the objects in the scene, but they also degrade the phase information in SAR images. SAR images are complex-valued images, and the phase information of SAR images is valuable for some SAR applications, such as SAR Interferometry. In SAR Interferometry, the relative phase between SAR images of the scene collected by platforms at slightly different positions is used for estimating the height of the scene.

Many techniques were proposed to solve the autofocus problem in SAR imaging [28] [30]. Recently, Sparsity-Driven Autofocus [20] (SDA) was proposed as a solution to autofocus. SDA is a regularization-based image reconstruction technique. In addition to using ℓ_1 -norm regularization to enforce scene sparsity, it solves the phase error problem due to motion errors by updating the initially assumed observation matrix with an estimated phase during image formation. The effectiveness of SDA was shown in terms of autofocus. SDA works on individual data collections, and does not have a mechanism for taking into account inter-channel information between interferometric image pairs, such as common sparsity.

For preservation of the inter-channel information in IfSAR, several joint image enhancement algorithms were proposed. One such approach is ℓ_1 regularization via complex approximate message passing [29]. This algorithm solves a joint optimization problem with a joint sparsity penalty term by using complex approximate message passing. Previously, Ramakrishnan et al. introduced the Joint Enhancement by Dual Descent Method [23], a joint image enhancement method with a

pixel-level equality constraint on reflectivity magnitudes of IfSAR image pairs. This image reconstruction algorithm enables the use of inter-channel information with this constraint while using sparsity penalties on each image. However, neither of these techniques provides a solution to the autofocusing problem. Another algorithm, joint image enhancement by iterative thresholding [19], was proposed by Muirgrew et al. In this approach, the enhancement problem over interferometric images is solved by iterative hard thresholding [6] and the autofocus problem is solved by an observation matrix update.

In order to deal with autofocusing while preserving the inter-channel information across acquisitions, we propose a new approach, Sparsity-Driven Coupled Imaging and Autofocusing (SDCIA). Our technique consists of a combination of the Joint Enhancement by Dual Descent Algorithm [23] and Sparsity-Driven Autofocus. [20] Our coupled optimization formulation involves a sparsity enforcing penalty term for each image, a term penalizing differences of reflectivity magnitudes at pairs of pixels in the IfSAR images, as well as the phase as an explicit variable of optimization in the observation matrix to eliminate phase errors caused by demodulation time uncertainties.

3.2 Proposed Method

In this section, we present our proposed technique, Sparsity-driven Coupled Imaging and Autofocusing (SDCIA), which involves a combination of the ideas involved in Joint Enhancement by Dual Descent Method [23] and Sparsity Driven Autofocus [20]. As mentioned previously, Joint Enhancement by Dual Descent Method [23] enables the preservation of inter-channel information in IfSAR by adding an equality constraint on image reflectivity magnitudes within the context of an ℓ_1 optimization problem for image enhancement. As a solution to the autofo-

cusing problem, Özben and Çetin introduced Sparsity Driven Autofocus [20]. This method handles phase errors by updating the observation matrix during sparsity-driven image reconstruction. It has been shown that this method alleviates the defocusing problem due to phase errors successfully. The method we present in this paper can handle both of these problems simultaneously.

SDCIA is a regularization-based image reconstruction and autofocusing technique that couples the two interferometric channels. Mathematically, it solves the following optimization problem:

$$\min_{f_1, f_2, \phi_1, \phi_2} L(f_1, f_2, \phi_1, \phi_2) \quad (3.1)$$

where

$$L(f_1, f_2, \phi_1, \phi_2) = \|g_1 - C_1(\phi_1)f_1\|_2^2 + \|g_2 - C_2(\phi_2)f_2\|_2^2 + \lambda_1^2 \|f_1\|_1 + \lambda_2^2 \|f_2\|_1 \quad (3.2)$$

subject to a pixel-based equality constraint on the magnitudes of the reflectivities of the two SAR images $|(f_1)_i| = |(f_2)_i|$ where $i = (1 \dots N)$ where N is the number of pixels. Here g_1 , g_2 , and C_1 , C_2 are the observed data and the observation matrices, respectively, for the first and the second acquisitions. The observation matrices depend on unknown phases ϕ_1 and ϕ_2 to be optimized for autofocusing. λ_1 and λ_2 are sparsity regularization parameters. The images involved in SAR Interferometry are expected to belong to the same scene and it is assumed they are registered images. Therefore, we set the two sparsity parameters as equal in our experiments.

Our procedure to solve the optimization problem in Eqn. (3.1) consists of two major steps in each iteration. In the first step, the Lagrangian method described in [23] is used to optimize the cost function in terms of f_1 and f_2 . Then, in the second step, the unknown phases are updated by using the corresponding steps

in the Sparsity Driven Autofocus method [20]. The overall process is summarized in Algorithm 1. The details of the two major update steps are described in the following two subsections.

Algorithm 1 Sparsity-driven Coupled Imaging and Autofocusing

Initilize $n = 0$, $f_1^{(0)} = C_1^H g_1$, $f_2^{(0)} = C_2^H g_2$, $C_1(\phi_1^{(0)}) = C_1$, $C_2(\phi_2^{(0)}) = C_2$, $\beta^{(0)} = 0$

1. Update f_1 and f_2 as follows:
 $f_1^{(n+1)}, f_2^{(n+1)} = \operatorname{argmin}_{f_1, f_2} L(f_1, f_2, \phi_1^{(n)}, \phi_2^{(n)})$
2. Update ϕ_1 and ϕ_2 as follows:
 $\phi_1^{(n+1)} = \operatorname{argmin}_{\phi_1} L(f_1^{(n+1)}, \phi_1)$
 $\phi_2^{(n+1)} = \operatorname{argmin}_{\phi_2} L(f_2^{(n+1)}, \phi_2)$
3. Update $C_1(\phi_1^{n+1})$ and $C_2(\phi_2^{n+1})$ by using ϕ_1^{n+1} , ϕ_2^{n+1} , C_1 , and C_2
4. Update β as shown in Equation (3.21)
5. Set $n = n + 1$, and repeat the procedure

Continue until relative changes in f_1 and f_2 are lower than predetermined thresholds, δ_1 and δ_2 .

3.2.1 Updating the Images

In each iteration of Algorithm 1 we update the SAR images by optimizing the cost function, $L(f_1, f_2, \phi_1, \phi_2)$, with respect to f_1 and f_2 . Mathematically, this is expressed as follows:

$$f_1^{(n+1)}, f_2^{(n+1)} = \operatorname{argmin}_{f_1, f_2} L(f_1, f_2, \phi_1^{(n)}, \phi_2^{(n)}) \quad (3.3)$$

subject to the constraint $|(f_1)_i| = |(f_2)_i|$. As described in [23], this constrained optimization problem can be converted into an unconstrained optimization problem, as we briefly discuss below. In this formulation, the constraints are included

in the objective function as Lagrange multiplier terms. Then, the optimization problem becomes:

$$\underset{\beta}{\operatorname{argmax}} \underset{f_1, f_2}{\operatorname{argmin}} L(f_1, f_2, \phi_1^{(n)}, \phi_2^{(n)}, \beta) \quad (3.4)$$

where $\beta = [\beta_1, \dots, \beta_N]^T$. The cost function, $L(f_1, f_2, \phi_1^{(n)}, \phi_2^{(n)}, \beta)$ is given by:

$$\begin{aligned} L(f_1, f_2, \phi_1^{(n)}, \phi_2^{(n)}, \beta) = & \left\| g_1 - C_1(\phi_1^{(n)})f_1 \right\|_2^2 + \left\| g_2 - C_2(\phi_2^{(n)})f_2 \right\|_2^2 + \\ & \lambda_1^2 \|f_1\|_1^1 + \lambda_2^2 \|f_2\|_1^1 + \sum_{n=1}^N \beta_i (|(f_1)_i|^2 - |(f_2)_i|^2) \end{aligned} \quad (3.5)$$

As shown by Ramakrishnan et al. [23], the derivative of this cost function with respect to f_1 and f_2 can be written as follows:

$$\nabla L(f_1, f_2)_{f_1} = [2C_1(\phi_1^{(n)})^H C_1(\phi_1^{(n)}) + p\lambda_1^2 \Lambda_1 + 2B]f_1 - 2C_1(\phi_1^{(n)})^H g_1 \quad (3.6)$$

$$\nabla L(f_1, f_2)_{f_2} = [2C_2(\phi_2^{(n)})^H C_2(\phi_2^{(n)}) + p\lambda_2^2 \Lambda_2 - 2B]f_2 - 2C_2(\phi_2^{(n)})^H g_2 \quad (3.7)$$

where the matrices used in Eqns. (3.6) and (3.7) are given by:

$$B = \begin{bmatrix} \beta_1 & & \\ & \ddots & \\ & & \beta_N \end{bmatrix} \quad \left| \begin{array}{l} \Lambda_1 = \operatorname{diag} \left\{ \frac{1}{(|(f_1)_i|^2 + \epsilon)^{1-\frac{p}{2}}} \right\} \\ \Lambda_2 = \operatorname{diag} \left\{ \frac{1}{(|(f_2)_i|^2 + \epsilon)^{1-\frac{p}{2}}} \right\} \end{array} \right| \quad i = 1, 2, \dots, N$$

where the parameter, ϵ , used in Λ_1 and Λ_2 is a small constant, usually 10^{-5} , to avoid problems due to nondifferentiability of the ℓ_1 norm at the origin. To solve for f_1 and f_2 , given a particular value of $\beta^{(n)}$ at iteration n , one can write the following fixed-point iterations, which can be shown to be equivalent to a quasi-Newton algorithm:

$$[2C_1(\phi_1^{(n)})^H C_1(\phi_1^{(n)}) + p\lambda_1^2 \Lambda_1^{(n)} + 2B^{(n)}] f_1^{(n+1)} = 2C_1(\phi_1^{(n)})^H g_1 \quad (3.8)$$

$$[2C_2(\phi_2^{(n)})^H C_2(\phi_2^{(n)}) + p\lambda_2^2 \Lambda_2^{(n)} - 2B^{(n)}] f_2^{(n+1)} = 2C_2(\phi_2^{(n)})^H g_2 \quad (3.9)$$

In order to solve the linear sets of equations in Eqns. (3.8) and (3.9), the conjugate gradient method can be used.

3.2.2 Updating the Phases and the Observation Matrices

After updating f_1 and f_2 in each iteration of Algorithm 1, the phase errors for each aperture position m of the two data acquisitions are updated. Mathematically, this can be expressed as follows:

$$\Delta\phi_{1m}^{(n+1)} = \underset{\Delta\phi_{1m}}{\operatorname{argmin}} L(f_1^{(n+1)}, \Delta\phi_{1m}) \quad (3.10)$$

$$\Delta\phi_{2m}^{(n+1)} = \underset{\Delta\phi_{2m}}{\operatorname{argmin}} L(f_2^{(n+1)}, \Delta\phi_{2m}) \quad (3.11)$$

These equations can be rewritten as follows:

$$\Delta\phi_{1m}^{(n+1)} = \underset{\Delta\phi_1}{\operatorname{argmin}} \left\| g_{1m} - \exp(j\Delta\phi_1) C_{1m}(\phi_1^{(n)}) f_1^{(n+1)} \right\|_2^2 \quad (3.12)$$

$$\Delta\phi_{2m}^{(n+1)} = \underset{\Delta\phi_2}{\operatorname{argmin}} \left\| g_{2m} - \exp(j\Delta\phi_2) C_{2m}(\phi_2^{(n)}) f_2^{(n+1)} \right\|_2^2 \quad (3.13)$$

where $\Delta\phi_{1m}^{(n+1)}$ and $\Delta\phi_{2m}^{(n+1)}$ are the phase error estimates at iteration $n + 1$ corresponding to the m^{th} aperture position of the first and second acquisitions, respectively. Similarly, g_{1m} , g_{2m} , $C_{1m}(\phi^{(n)})$, $C_{2m}(\phi^{(n)})$ are the parts of the collected data and observation matrix which are related to the m^{th} position of the first and second acquisitions. The cost functions in Eqns. (3.12) and (3.13) can also be written as follows (see Appendix A for detailed explanation): [20]

$$\Delta\phi_{1m}^{(n+1)} = \underset{\Delta\phi_1}{\operatorname{argmin}} \left(g_m^H g_m - 2\sqrt{R_1^2 + I_1^2} \cos[\Delta\phi_1 + \arctan(\frac{-I_1}{R_1})] \right. \\ \left. + f_1^{(n+1)H} C_{1m}(\phi_1^{(n)})^H C_{1m}(\phi_1^{(n)}) f_1^{(n+1)} \right) \quad (3.14)$$

$$\Delta\phi_{2m}^{(n+1)} = \underset{\Delta\phi_2}{\operatorname{argmin}} \left(g_m^H g_m - 2\sqrt{R_2^2 + I_2^2} \cos[\Delta\phi_2 + \arctan(\frac{-I_2}{R_2})] \right. \\ \left. + f_2^{(n+1)H} C_{2m}(\phi_2^{(n)})^H C_{2m}(\phi_2^{(n)}) f_2^{(n+1)} \right) \quad (3.15)$$

where

$$R_1 = \operatorname{Re}\{f_1^{(n+1)H} C_{1m}(\phi_1^{(n)})^H g_{1m}\}, \quad R_2 = \operatorname{Re}\{f_2^{(n+1)H} C_{2m}(\phi_2^{(n)})^H g_{2m}\} \quad (3.16)$$

$$I_1 = \operatorname{Im}\{f_1^{(n+1)H} C_{1m}(\phi_1^{(n)})^H g_{1m}\}, \quad I_2 = \operatorname{Im}\{f_2^{(n+1)H} C_{2m}(\phi_2^{(n)})^H g_{2m}\} \quad (3.17)$$

These minimization problems can be solved by maximizing the cosine term inside the cost functions. This can be achieved by setting $\Delta\phi_1$ and $\Delta\phi_2$ as follows, because cosine reaches its maximum when its argument is equal to 0.

$$\Delta\phi_{1m}^{(n+1)} = -\arctan\left(\frac{-I_1}{R_1}\right), \quad \Delta\phi_{2m}^{(n+1)} = -\arctan\left(\frac{-I_2}{R_2}\right) \quad (3.18)$$

Next, the phases and observation matrices will be updated by adding $\Delta\phi_1$ and

$\Delta\phi_2$ to the current phase estimates:

$$\phi_{1m}^{(n+1)} = \Delta\phi_{1m}^{(n+1)} + \phi_{1m}^{(n)} , \quad \phi_{2m}^{(n+1)} = \Delta\phi_{2m}^{(n+1)} + \phi_{2m}^{(n)} \quad (3.19)$$

$$C_{1m}^{(n+1)}(\phi_1) = \exp(j\Delta\phi_{1m})C_{1m}^{(n)}(\phi_1) , \quad C_{2m}^{(n+1)}(\phi_2) = \exp(j\Delta\phi_{2m})C_{2m}^{(n)}(\phi_2) \quad (3.20)$$

As another minor step in each iteration, the Lagrange multiplier vector $\beta^{(n)}$ is updated as follows:

$$\beta^{(n+1)} = \beta^{(n)} + \alpha \nabla \xi(\beta^{(n)}) \quad (3.21)$$

where α is the step size specified by the user. $\nabla \xi(\beta^{(n)})$ is the gradient of the cost function Eqn. (3.5):

$$\nabla \xi(\beta^{(n)}) = |\hat{f}_1^{(n)}|^2 - |\hat{f}_2^{(n)}|^2. \quad (3.22)$$

This iterative process will continue until a convergence criterion is satisfied. In our experiments, the relative change in the reconstructed image reflectivities is considered as a stopping metric. The relative change is calculated as follows:

$$\frac{\left\| f_1^{(n+1)} - f_1^{(n)} \right\|^2}{\left\| f_1^{(n)} \right\|^2} < \delta_1 , \quad \frac{\left\| f_2^{(n+1)} - f_2^{(n)} \right\|^2}{\left\| f_2^{(n)} \right\|^2} < \delta_2 \quad (3.23)$$

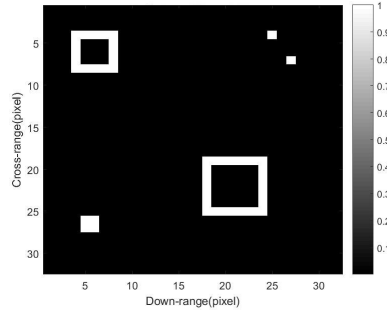
When this change goes below a pre-determined threshold for each image, the algorithm stops. We define the stopping threshold as 0.001 in our experiments.

3.3 Simulation Results

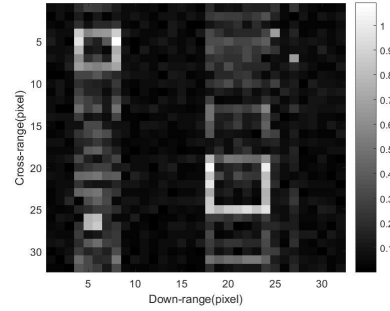
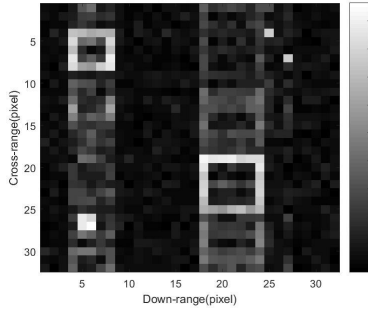
In order to show the effectiveness of our algorithm, the results of experiments done on synthetic scenes are presented. The purpose of the first two experiments is to compare the performance of Joint Enhancement by Dual Descent Algorithm [23], SDA [20], and SDCIA when both acquisitions are affected by motion errors. The synthetic scene used in Test 1 and Test 2 can be seen in Figure 3.1a. This scene consists of several point and geometric objects as well as minor clutter in the background. The reflectivities of the objects were set to 1, and a phase of 180 degrees, was added to the reflectivities of the objects in the scene used for the second image. Therefore, a phase difference between the first and the second images is expected to be observed in the reconstructions. The parameters used in this synthetic imaging experiment are shown in Table 3.1. We distort the phase history data of the first and second acquisitions by adding random phase errors as well as Gaussian noise to these phase histories resulting in an SNR of 25 dB. The images reconstructed by the polar format algorithm (PFA) are shown in Figures 3.1b and 3.1c.

Table 3.1: The values of the imaging parameters used in the simulations.

Parameters	Values
Center Frequency (ω_0)	$2\pi * 10^{10} \text{ rad/sec}$
Bandwidth	400 MHz
Pulse Duration	$4 * 10^4 \text{ sec}$
Chirp Rate	$2\pi * 10^{12} \text{ rad/sec}$



(a) Synthetic scene used in the experiments.



(b) The first image generated by PFA.

(c) The second image generated by PFA.

Figure 3.1: Synthetic scene used in the first two experiments and the SAR images generated by the Polar Format Algorithm.

The results our approach as well as the two existing methods can be seen in Figures 3.2 and 3.3. Here, the enhanced first and second images of the algorithms and the relative phase plots are presented. The relative phase plots are generated as follows. Since the exact location of the scatterers is known, we applied a mask over the enhanced images to keep only the pixel values corresponding to object scatterer locations. Then, the relative phase was calculated by multiplying the first images with complex conjugate of the second images. The relative phase values are plotted with respect to their downrange locations.

In Figure 3.2, the results of the first experiment are shown. The algorithm parameters, λ_1^2 , λ_2^2 , and step size α , are selected as 2, 2, 0.000005. Here, the blurring in the cross-range direction, due to phase errors in the data, is observed

in the output images of the Joint Enhancement by Dual Descent Algorithm and the Sparsity-Driven Autofocus Algorithm. Such degradation in the formed imagery also affect the relative phase information between the images as shown in Figures 3.2c and 3.2f. On the other hand, SDCIA obtains relatively better results than the other two algorithms with the same parameters both in terms of focusing and relative phase information preservation.

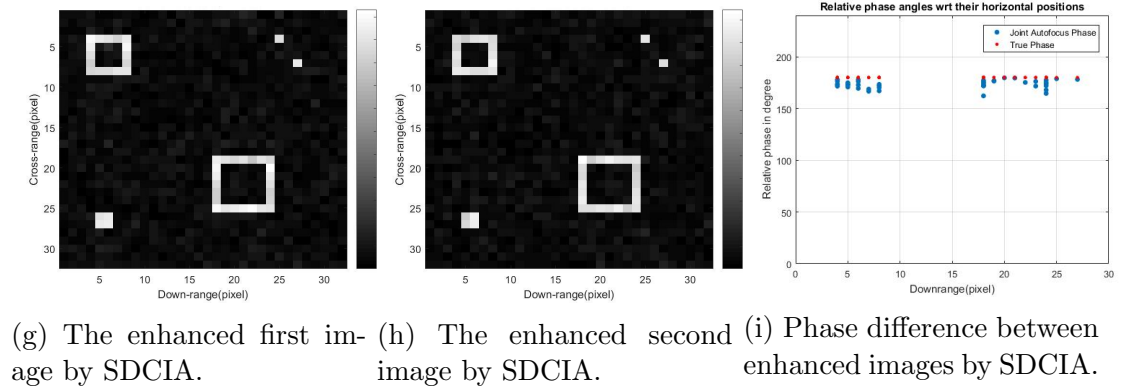
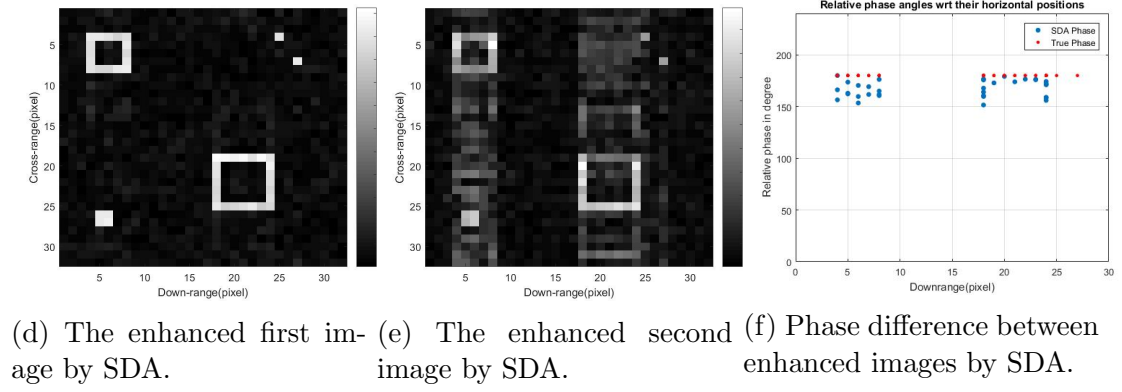
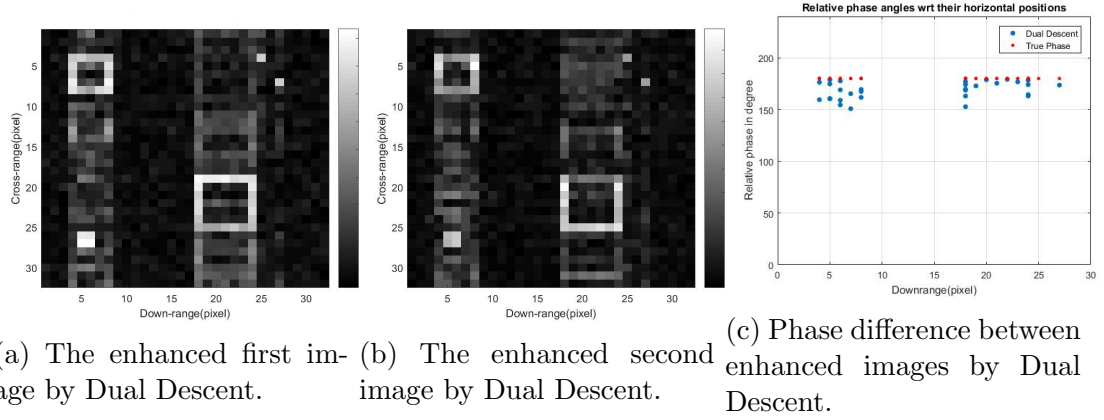


Figure 3.2: The results of the first experiment. The parameters λ_1^2 , λ_2^2 , and α are chosen empirically as 2, 2, and 0.000005. In the relative phase plots, true phase difference values are shown as red points, and phase differences estimated by each algorithm are shown as blue points.

The results of the second experiment can be seen in Figure 3.3. In this experiment, λ_1^2 , λ_2^2 , and α are set to 3, 3, and 0.000005. With these parameters, we can easily see that SDA exhibits better performance in terms of focusing compared to the previous experiment. Its performance with regard to preserving relative phase information also approaches that of SDCIA. As the value of the sparsity regularization parameters, λ_1 and λ_2 , increase, we force the algorithm to find more sparse solutions. If the sparsity terms are increased too much, the cost due to the equality constraint will have a smaller effect on the total cost function. Therefore, SDA and SDCIA may produce similar outputs when strong sparsity constraints are imposed. Whether such parameter values are desirable depends on the scene, because the assumption of strong spatial sparsity may not be valid for all scenes. The scene may contain features that are not spatially sparse. In such cases, the equality constraint can provide additional and useful information. Therefore, parameter choices should be based on prior information about the scene.

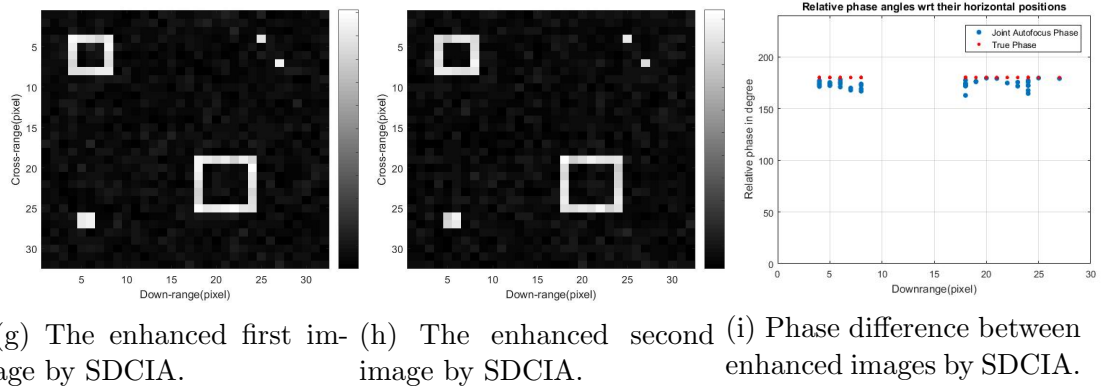
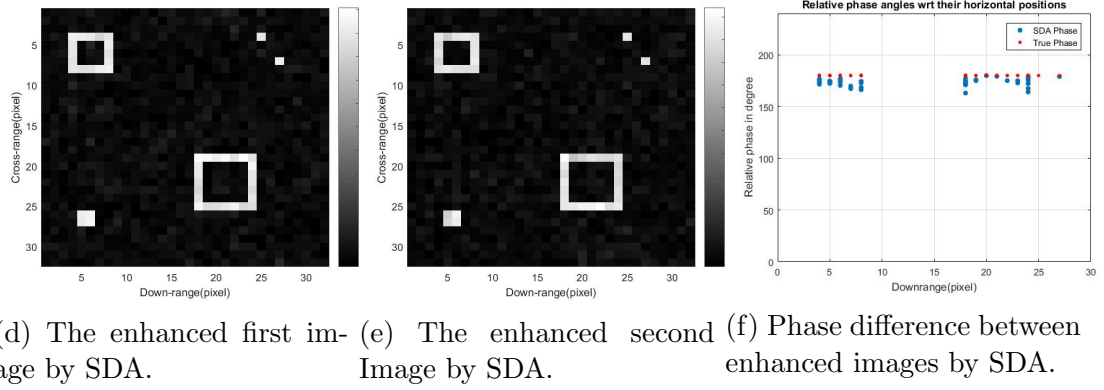
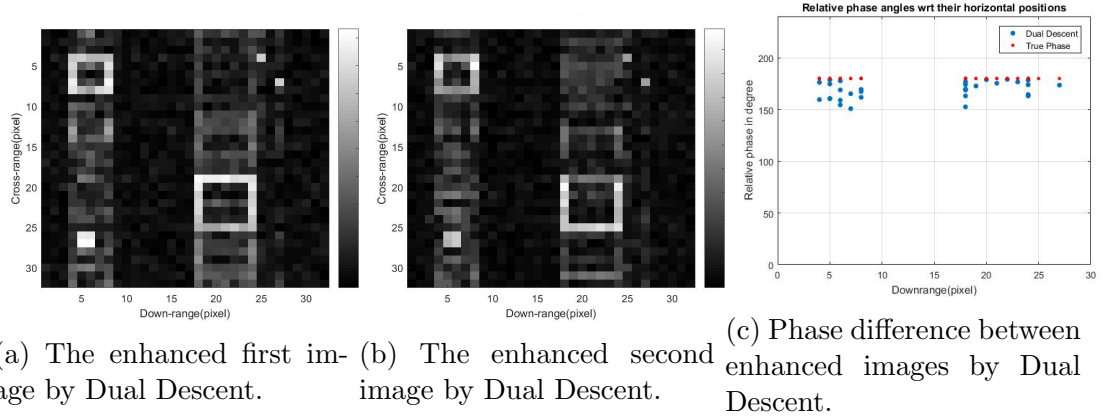
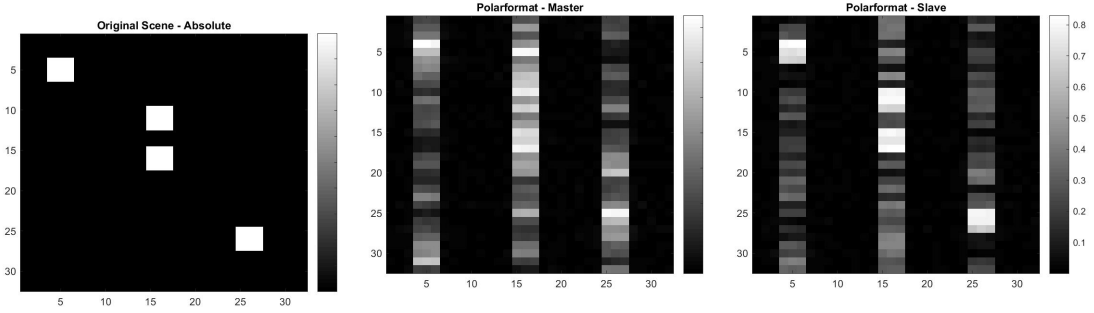


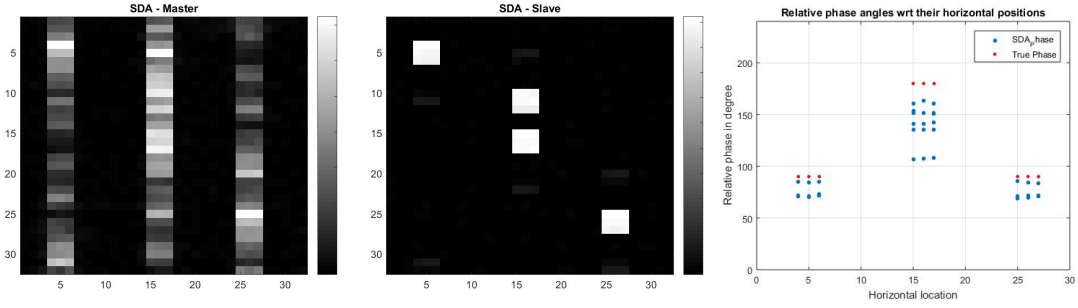
Figure 3.3: The results of the second experiment. The parameters λ_1^2 , λ_2^2 , and α are chosen empirically as 3, 3, and 0.000005. In the relative phase plots, true phase difference values are shown as red points, and phase differences estimated by each algorithm are shown as blue points.



(a) Original Scene.

(b) The first image formed by PFA.

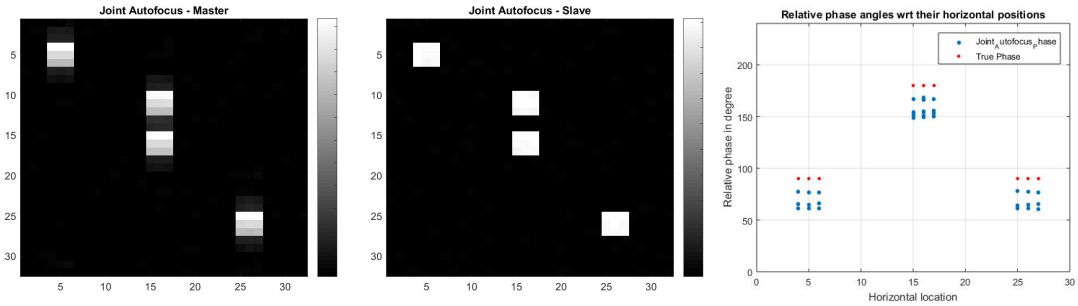
(c) The second image formed by PFA.



(d) The enhanced first image by SDA.

(e) The enhanced second image by SDA.

(f) Phase difference between enhanced images by SDA.

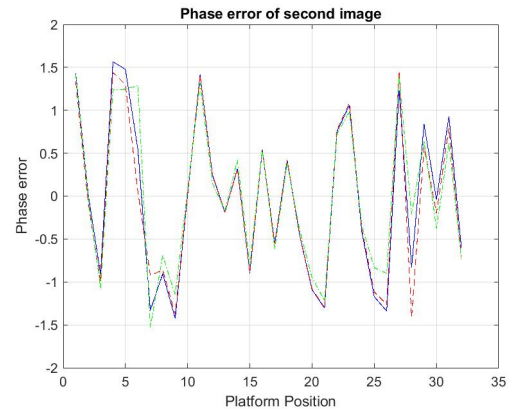
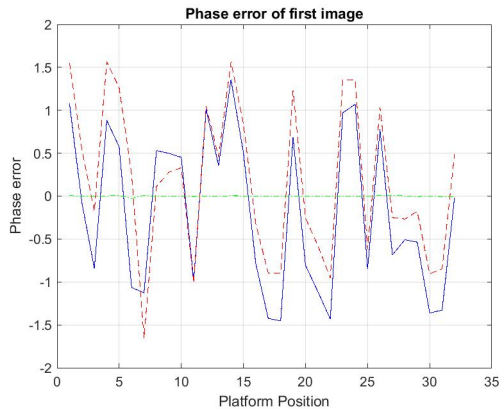


(g) The enhanced first image by SDCIA.

(h) The enhanced second image by SDCIA.

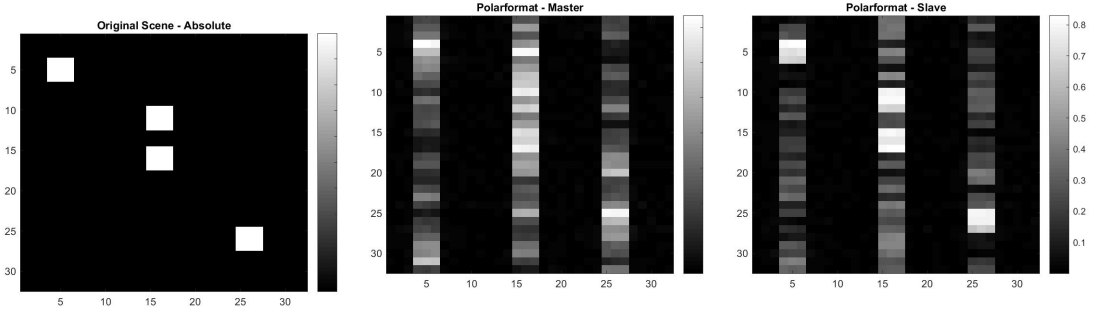
(i) Phase difference between enhanced images by SDCIA.

Figure 3.4: The results of the third experiment. The parameters λ_1^2 , λ_2^2 , and α are chosen empirically as 2, 2, and 0.00005. In the relative phase plots, true phase difference values are shown as red points, and phase differences estimated by each algorithm are shown as blue points.



(a) Phase error estimates for the first image (b) Phase error estimates for the second image in Test 3.

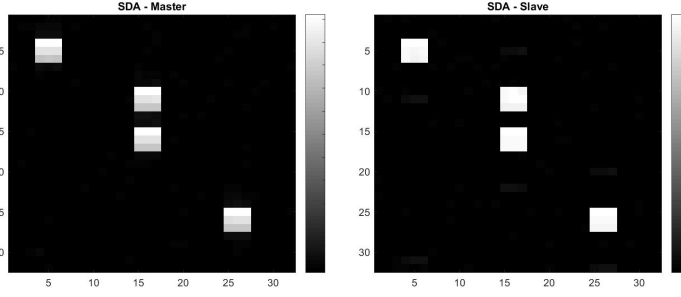
Figure 3.5: The phase error estimates for Test 3. The blue solid curve represents the true phase error. The red dashed and green dash-dotted curves represent the phase error estimates obtained by SDCIA and SDA, respectively.



(a) Original Scene.

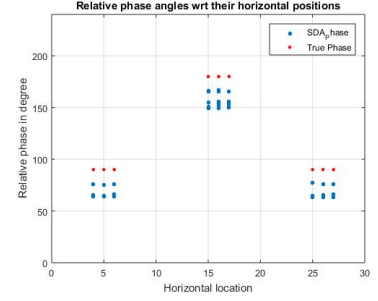
(b) The first image formed by PFA.

(c) The second image formed by PFA.

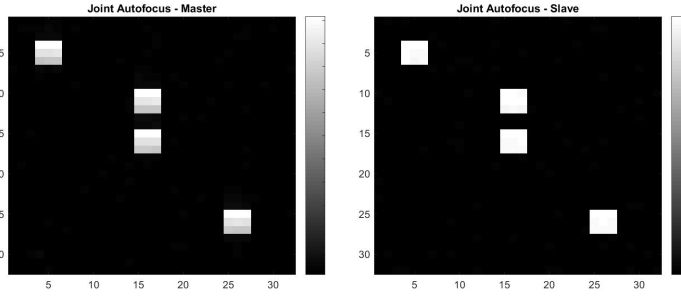


(d) The enhanced first image by SDA.

(e) The enhanced second image by SDA.

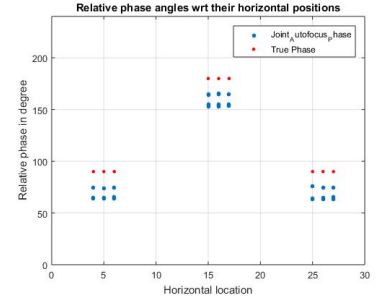


(f) Phase difference between enhanced images by SDA.



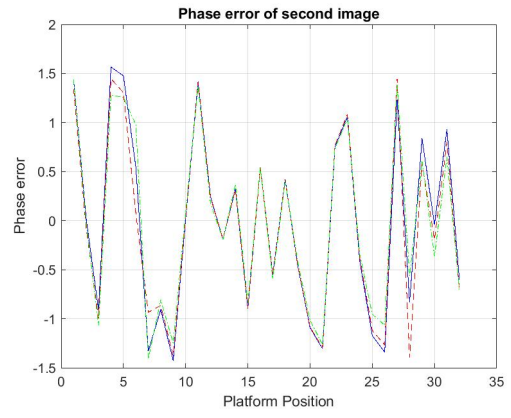
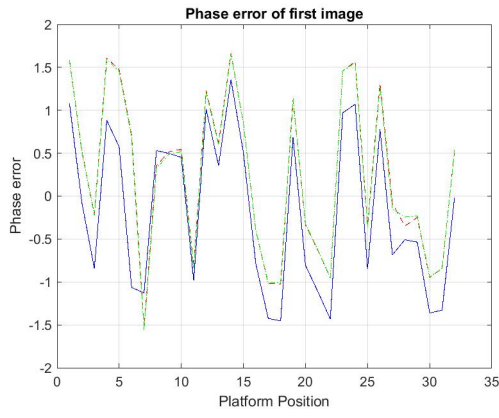
(g) The enhanced first image by SDCIA.

(h) The enhanced second image by SDCIA.



(i) Phase difference between enhanced images by SDCIA.

Figure 3.6: The results of the fourth experiment. The parameters λ_1^2 , λ_2^2 , and α are chosen empirically as 3, 3, and 0.00005. In the relative phase plots, true phase difference values are shown as red points, and phase differences estimated by each algorithm are shown as blue points.



(a) Phase error estimates for the first image (b) Phase error estimates for the second image in Test 4.

Figure 3.7: The phase error estimates for Test 3. The blue solid curve represents the true phase error. The red dashed and green dash-dotted curves represent the phase error estimates obtained by SDCIA and SDA, respectively.

In the next two experiments, Test 3 and 4, we compare SDCIA and SDA in term of their phase error estimates. For this purpose, we use the images shown in Figures 3.4b and 3.4c. Each of them are equally degraded by motion errors. We reconstruct the scenes with SDCIA and SDA. The parameters λ_1^2 , λ_2^2 , and α are chosen empirically as 2, 2, and 0.00005. The results are presented in Figure 3.4. In addition, the phase error estimates of the methods are presented in Figure 3.5. When we take a look at Figures 3.4 and 3.5, the results of SDCIA are better than SDA both in terms of focusing and in terms of phase error estimation. We repeat this scenario with a different set of parameter selections. In Test 4, The parameters λ_1^2 , λ_2^2 , and α are selected as 3, 3, and 0.00005. The output images and phase error estimates are shown in Figures 3.6 and 3.7, respectively. With these parameter choices, we can state that the performances of the methods are very close. Based on these results, it appears that SDCIA exhibits good performance with a wider range of sparsity parameters than SDA.

The aim of the fifth and sixth tests is to show the effectiveness of SDCIA in a different scenario. The scene used for Test 5 and Test 6 can be seen in Figure 3.8a. In this scenario, one of the acquisitions is exposed to more motion and noise errors than the other one. To exploit this information, we modify SDCIA so that it updates only the image with higher error and keeps the other image fixed through its iterations. The idea is that through the equality constraint, the image with low error may provide useful information for enhancing the image with higher error. In other scenarios, one might similarly consider keeping a subset of the variables constant and updating the others in SDCIA. For example, if we know that the first acquisition is not degraded by motion errors, but only by measurement noise, we might remove ϕ_1 only from the optimization process and update all the other variables.

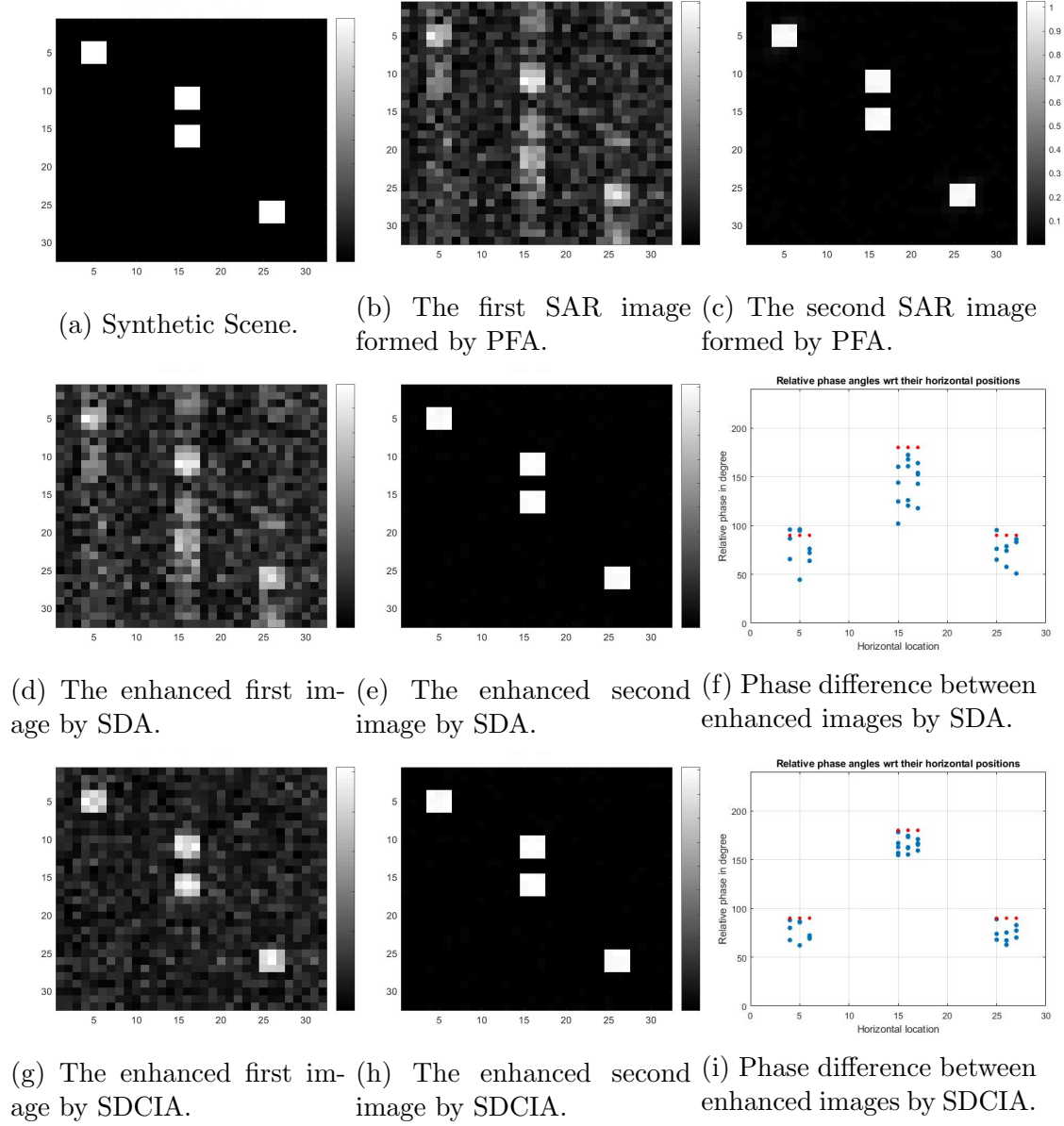
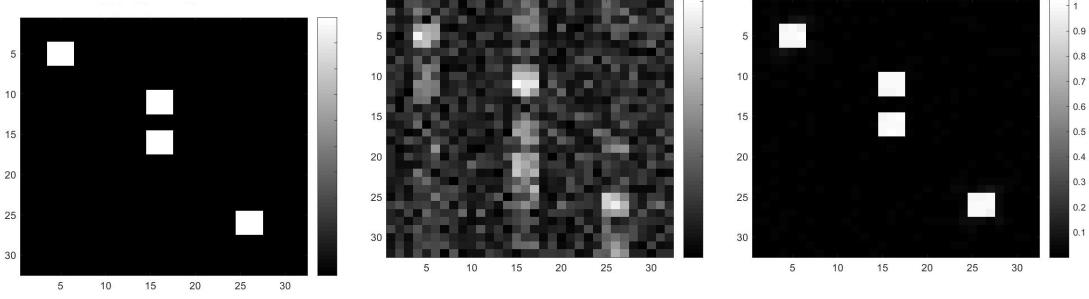


Figure 3.8: The results of the fifth experiment. The parameters λ_1^2 , λ_2^2 , and α are empirically chosen as 2, 2, and 0.5. In the relative phase plots, true phase difference values are shown as red points, and phase differences estimated by each algorithm are shown as blue points.

In the experiment performed here, random phase errors and noise resulting in 0 dB SNR are added to the phase history data of the first acquisition. In the second acquisition, SNR is 25 dB and no phase errors are present. The images formed by PFA from the noisy first acquisition and the less noisy second acquisition are shown in Figures 3.8b and 3.8c. Other results of Test 5 are presented in the rest of Figure 3.8. λ_1^2 , λ_2^2 , and α are set to 2, 2, and 0.5, respectively. Similar to the results obtained from Test 1, SDCIA exhibits better performance than SDA in terms of focusing and relative phase preservation.

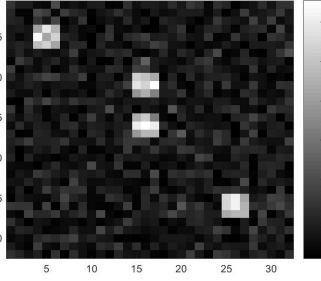
In the sixth experiment, the scenario used in Experiment 5 was repeated with different parameters. λ_1^2 , λ_2^2 , and α were set to 40, 40, and 0.5. The results of Experiment 6 are presented in Figure 3.9. With these parameters, the performance of SDA approaches that of SDCIA. This is due to the use of relatively higher sparsity parameters than those used in Experiment 5. In this case, SDA needs to use higher values to produce accurate sparse outputs. However, SDCIA can produce focused images with lower sparsity parameters, and in fact with a wide range of sparsity parameters, with the help of the equality constraint. In order to quantitatively evaluate the performance in relative phase preservation, the phase RMSE values of SDA and SDCIA were calculated for different sparsity parameters and are shown in Figure 3.10. Consistently with the qualitative results presented, SDCIA performs relatively better than SDA. As the sparsity parameter increases, the performance of SDA approaches that of SDCIA.



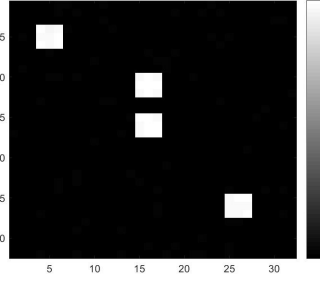
(a) Synthetic Scene.

(b) The first SAR image formed by PFA.

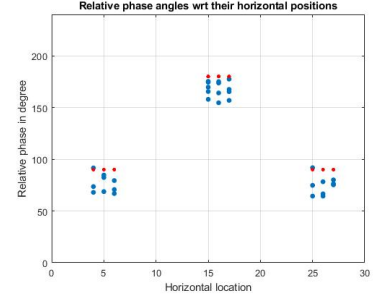
(c) The second SAR image formed by PFA.



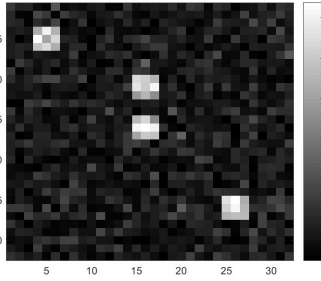
(d) The enhanced first image by SDA.



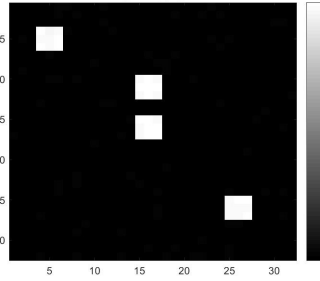
(e) The enhanced second image by SDA.



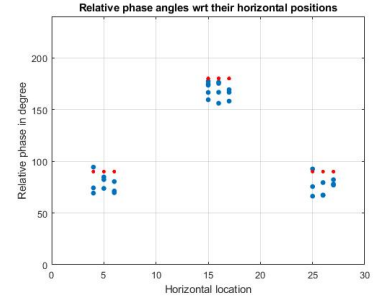
(f) Phase difference between enhanced images by SDA.



(g) The enhanced first image by SDCIA.



(h) The enhanced second image by SDCIA.



(i) Phase difference between enhanced images by SDCIA.

Figure 3.9: The results of the sixth experiment. The parameters λ_1^2 , λ_2^2 , and α are chosen empirically as 40, 40, and 0.5. In the relative phase plots, true phase difference values are shown as red points, and phase differences estimated by each algorithm are shown as blue points.

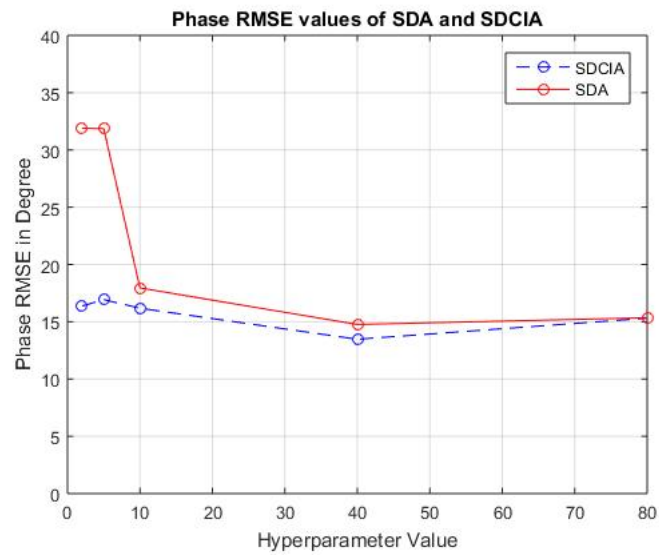


Figure 3.10: Phase RMSE values of SDA and SDCIA algorithms for different sparsity parameters.

Chapter 4

SAR Interferometry Toolbox Project

The purpose of this chapter is to summarize the work done for the SAR Interferometry Toolbox Project, and the algorithms involved in each component of the SAR Interferometry Toolbox.

4.1 Project Description

As a part of my master studies, I worked on an industry project, the SAR Interferometry Toolbox Project.

The main aim of this project was to produce a software toolbox which can perform SAR Interferometric processing on the data of the Göktürk-3 satellite. Göktürk-3 satellite project is planned as the first SAR satellite of Turkey. In the main undertaking of TAI, TUBITAK Space Research Institute and ASELSAN also served as subcontractors. This satellite is planned to be launched in 2019.

In addition to typical SAR imaging modalities, Göktürk-3 is planned to have SAR Interferometric imaging capability as well. In order to create a SAR Interfer-

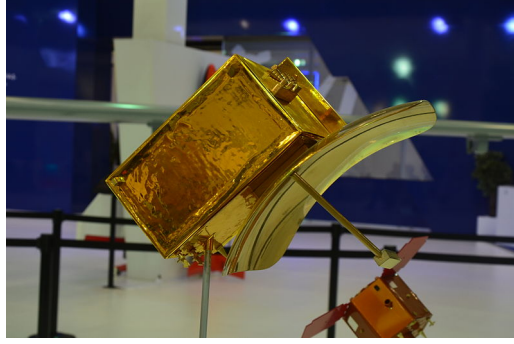


Figure 4.1: Model of Gökürk-3 displayed at the stand of TAI during the IDEF'15.

ometry processor for Gökürk-3, an effort has been initiated in 2015. Within this context, I was supported as a master student by ASELSAN. Within the framework of this project, we delivered detailed reports about SAR Interferometry, and a software toolbox which is capable of performing fundamental steps of SAR Interferometry processing.

4.2 SAR Interferometry Toolbox

The main objective of this project was to produce a software tool which can perform the fundamental steps of SAR Interferometry processing. In this context, the first version of this toolbox, SAR Interferometry Toolbox v.1., was delivered in 2017.

While working on the first version of the toolbox, our main concern has been to produce an end-to-end interferometric processor which can perform the primary steps of interferometric SAR processing to generate 3-D height maps as its output. This section contains comprehensive descriptions of the algorithms involved in each step of the process together with their input output relationships. In addition, our experimental results on sample data provide an initial picture of the performance in terms of product quality.

4.2.1 Algorithm Design

The this version of the toolbox described in this thesis is capable of performing the most fundamental steps of interferometric processing. The steps of interferometric processing we considered in our work are illustrated in Figure 4.2.

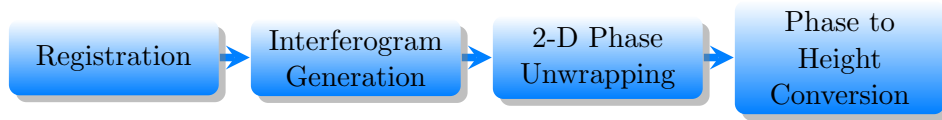


Figure 4.2: Components of the SAR Interferometry Toolbox.

Algorithm Inputs

The list of inputs required by the toolbox in order to create 3-D height maps is given in Table 4.1.

The SAR interferometry toolbox needs a pair of images of the scene of interest, namely the master and slave images, as its main inputs. In addition to data, some system parameters are also needed for interferometric processing. These parameters are listed in Table 4.1. In our basic interferometric processor described here, nominal baseline values specified by the data providers are used.

Name of Input	Input Type	Unit
Master Image	Complex Image	-
Slave Image	Complex Image	-
Wavelength	Parameter	Meters
Baseline	Parameter	Meters
Tilt Angle	Parameter	Degrees
Range	Parameter	Meters
Incidence Angle	Parameter	Degrees

Table 4.1: List of the inputs required by the toolbox.

Some algorithmic parameters, such as the dimension of the window used for

multilooking operation or oversampling factors, are not treated as global input parameters here. They are mentioned as user-specified inputs in the relevant sections.

Algorithm Description

In this section we describe the algorithms used in the first version of the SAR interferometry toolbox for each step illustrated in Figure 4.2. This toolbox is able to perform the most crucial interferometric processing steps. In this section, we provide a detailed description of our algorithms for each step.

Registration The registration algorithm we use in the toolbox consists of two steps: coarse and fine registration. The pseudocode of the algorithm is given in Algorithm 1.

In coarse registration, relative shifts in range and azimuth directions are determined approximately by using reference points in the master and slave images. In the case that input images are geolocated, this step may not be necessary. These reference points can be determined by visual inspection or by an automated algorithm. In SAR Interferometry Toolbox, manual selection is performed. Even though this procedure would provide an estimate of relative shifts in both directions, it would not satisfy the sub-pixel accuracy condition in most scenarios.

After that, fine registration is applied to achieve sub-pixel accuracy. Common regions determined in coarse registration are captured with windows, of, e.g., 100×100 pixels. Then, these windows are oversampled, usually with a factor of 8 [21]. The size of the windows and oversampling factor can be specified by users as input parameters. For oversampling, we used a function provided by DLR(German Aerospace Agency) that performs oversampling through zeropadding in the Fourier transform domain. The complex correlations of common regions of master and

slave images are calculated. Locations of the peaks in complex correlations correspond to the amount of shift between images. Although complex cross correlation techniques provide good results, they are computationally intensive. Using smaller windows can speed up the process.

Once the amount of shift is determined, the slave image can be transformed by a two-dimensional translation operation. In this version of the toolbox, we take into account only shifts in range and azimuth dimensions.

Algorithm 2 Registration Step (Translation only) for SAR Interferometry

```
1: procedure REGISTRATION
2:    $I_m \leftarrow$  Master Image
3:    $I_s \leftarrow$  Slave Image
4:    $s_{mi} \leftarrow$  Reference Points in master image
5:    $s_{si} \leftarrow$  Reference Points in slave image
6:    $r_{mi} \leftarrow$  Regions in the master image around reference points
7:    $r_{si} \leftarrow$  Regions in the slave image around reference points
8:    $numRef \leftarrow$  Number of reference points.
9:    $x_{mid} \ y_{mid} \leftarrow$  Coordinates of centre of reference area
10:   $M \leftarrow$  Oversampling Factor
11:  for  $i = 1:numRef$  do
12:     $s_i \leftarrow$  Determine reference points manually.
13:  end for
14:  for each:  $s_i$ 
15:     $r_{mi} \leftarrow$  Extracting the region around interest points in master image.
16:     $r_{si} \leftarrow$  Extracting the region around interest points in slave image.
17:    for  $i = 1:numRef$  do
18:       $w_{mi} = \text{fft}(r_{mi})$ 
19:       $w_{si} = \text{fft}(r_{si})$ 
20:       $o_{mi} = \text{zeropad2d}(w_{mi}, M)$ 
21:       $o_{si} = \text{zeropad2d}(w_{si}, M)$ 
22:       $t_{mi} = \text{ifft}(o_{mi})$ 
23:       $t_{si} = \text{ifft}(o_{si})$ 
24:       $p_i = \text{crosscorrelation}(t_{mi}, t_{si})$ 
25:       $[x_i \ y_i] \leftarrow$  Coordinates of the peak of cross correlation
26:    end for
27:     $x_{fine} = \text{average}(x_i - x_{mid})/8$ 
28:     $y_{fine} = \text{average}(y_i - y_{mid})/8$ 
29:     $[x_{coar} \ y_{coar}] = \text{average}(s_{mi} - s_{si})$ 
30:     $x_{tot} = x_{fine} + x_{coar}$ 
31:     $y_{tot} = y_{fine} + y_{coar}$ 
32:     $[\hat{I}_s] = \text{register}(I_s, x_{tot}, y_{tot})$ 
33:  return  $I_m \hat{I}_s$ 
34: end procedure
```

Interferogram Generation As discussed in some resources [16], phase differences between SAR images can be obtained by multiplying the first, or master,

SAR image with complex conjugate of second, or slave, image (or vice versa).

First, phase difference between complex images is calculated as shown in Equation (4.1). Basically, this is a multiplication of the master image and the complex conjugate of the slave image.

$$\varphi_{ML} = \angle \left(\sum_{n=1}^N u_1^* u_2 \right). \quad (4.1)$$

Since phase exhibits statistical behaviour, this multiplication yields only an ML estimate of the phase difference between two SAR images.

The step called complex multilooking is implemented by calculating this estimate. The precision and noise sensitivity of the phase estimate depend on the size of the window used in multilooking. In our simulations, we use a 5×5 window mostly, but this parameter can be changed in our toolbox based on user preferences.

Lastly, the flat earth component, phase contribution due to range, should be subtracted. As we stated in previous reports [33] [32], there are two main geometric parameters which affect phase: range and elevation. In other words, the phase difference between observations depends on the range values as well. Therefore, this component should be eliminated to obtain the phase difference due to height variations over the scene. This term, which is called the flat earth component, was provided in the dataset used in our initial experiments. In order to obtain initial results quickly, we directly used it. For real data, it can be calculated based on system parameters. This phase component is calculated as follows:

$$\delta r = \delta r_0 - \frac{b_{\perp}}{r_0} (r - r_0) \cot(\theta_i - \beta) \quad (4.2)$$

where δr , δr_0 , b_{\perp} , r_0 , r , θ_i , β are range difference between platforms, initial range difference, perpendicular baseline, range to center, range, incidence angle, and

local slope. SAR Interferometry Toolbox v.1 is capable of calculating the flat earth component of the scene.

Algorithm 3 Interferogram Calculation

```

1: procedure INTERFEROGRAM CALCULATION
2:    $I_m \leftarrow$  Registered Master Image
3:    $I_s \leftarrow$  Registered Slave Image
4:    $N \leftarrow$  Number of pixel used for multilooking operation
5:    $\hat{\varphi} = \angle \left( \sum_{n=1}^N \hat{I}_m^* \hat{I}_s \right)$ 
6:    $\hat{\varphi} = \hat{\varphi} - \text{Flat Earth Component}$ 
   return  $\hat{\varphi}$ .
7: end procedure

```

Another measure about the scene is the complex correlation coefficient, or coherence of the two SAR images, which can be estimated as follows:

$$\gamma_{MLE} = \frac{\sum_{n=1}^L u_1[n] u_2[n]^*}{\sqrt{\sum_{n=1}^L u_1[n]^2 \sum_{n=1}^L u_2[n]^2}} \quad (4.3)$$

where u_1 and u_2 are master and slave images respectively. Its phase is the expected interferometric phase of the pixel under discussion; its magnitude is related to phase noise. Receiver noise, for example, may render the two images to be not fully correlated, i.e. $|\gamma| < 1$ [3]. Hence, $|\gamma|$ can be used as an estimate of the degree of coherence, to generate a coherence map. We generate such a coherence map as an additional output of the first version of our toolbox. A 5×5 window is used in computing the coherence in our initial experiments.

2-D Phase Unwrapping In this toolbox, we have performed phase unwrapping using a simple procedure. In particular, as an initial attempt, we used an extended version of a 1-D phase unwrapping algorithm in order to produce initial 3-D models. The pseudocode of the underlying 1-D phase unwrapping algorithm is given in Algorithm 3.

The methodology of this simple 1-D phase unwrapping algorithm is as follows. This algorithm detects the locations in the input vector (1-D image) where wrapping occurs by calculating the phase gradient between neighbourhood pixels. If there is a phase difference between neighbourhood pixels above the upper or below the lower threshold (in our case these thresholds are π and $-\pi$) this means that phase is wrapped at this point. Based on the sign of the phase gradient, -2π or 2π phase is added to the phase vector.

Algorithm 4 1-D Phase Unwrapping

```

1: procedure 1-D PHASE UNWRAPPING ALGORITHM
2:    $I \leftarrow$  Wrapped Vector,  $1 \times N$ 
3:    $U \leftarrow$  Unwrapped Vector,  $1 \times N$ 
4:    $numCycle \leftarrow$  The vector that determines how many cycles should be added.
5:    $numCycle = zeros(1, N)$ 
6:   for  $j = 1:N-1$  do
7:      $\Delta = I(j) - I(j+1)$ 
8:     if  $\Delta > \pi$  then
9:        $numCycle(j+1:N) = numCycle(j+1:N) - 1$ 
10:    else if  $\Delta < -\pi$  then
11:       $numCycle(j+1:N) = numCycle(j+1:N) + 1$ 
12:    end if
13:  end for
14:   $U = I + numCycle * 2\pi$  return  $U$   $numCycle$ .
15: end procedure

```

For 2-D phase unwrapping, we used an extended version of this 1-D phase unwrapping algorithm. In Algorithm 4, pseudocode of the algorithm is presented. There are two different approaches for extending Itoh's method to the 2-D phase unwrapping problem. Namely either columns or rows of the 2-D data can be used as the input of 1-D phase unwrapping algorithm. Then, 2-D unwrapping problem is reduced to multiple 1-D unwrapping problems which simplifies the problem.

Algorithm 5 Extension of 1-D Phase Unwrapping Algorithm for 2-D phase unwrapping problem

```

1: procedure 1-D PHASE UNWRAPPING ALGORITHM
2:    $I \leftarrow$  Wrapped interferogram
3:    $I_i \leftarrow$  Columns of wrapped interferogram
4:    $R_1 \leftarrow$  First row of wrapped interferogram
5:    $T_1 \leftarrow$  First row of unwrapped interferogram
6:    $numCol \leftarrow$  Number of columns of interferogram
7:    $U \leftarrow$  Unwrapped Interferogram
8:    $U_i \leftarrow$  Unwrapped Column Vector
9:    $[T_1, numCycle] = 1Dphaseunwrapper(R_1)$ 
10:  for  $i = 1 : numCol$  do
11:     $U_i = 1dphaseunwrapper(I_i)$ 
12:  end for
13:  for  $i = 1 : numCol$  do
14:     $U_i = U_i + 2\pi * numCycle(i)$ 
15:  end for
16:  return  $U$ .
17: end procedure

```

We should note that this simple method will not produce perfectly unwrapped interferograms because of the existence of the residue problem. Path following phase unwrapping algorithms are not immune to path-dependency. Residues make the unwrapping operation path-dependent, so the locations of residues should be determined to get consistent results. We plan to implement such an advanced algorithm for the next version of the toolbox.

Phase to Height Conversion Height conversion can be performed based on the unwrapped flattened phase.

The relationship between phase and height through phase sensitivity was stated as follows [3]:

$$\frac{d\phi}{dh} = \frac{4\pi}{\lambda} \frac{B_{\perp}}{R \sin(\theta_i)} \quad (4.4)$$

By rearranging Equation (4.4), relative height can be obtained from the un-

wrapped phase as follows

$$h = \frac{\lambda}{4\pi} \frac{R \sin(\theta_i) \phi}{B_{\perp}} \quad (4.5)$$

where λ , B_{\perp} , θ_i and R are the wavelength of the transmitted waveform, perpendicular baseline, incident angle, and range.

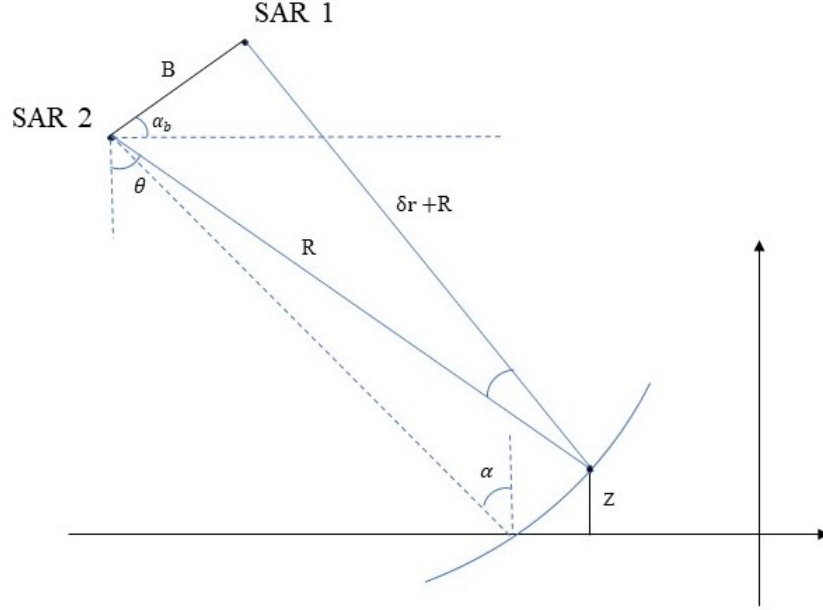


Figure 4.3: Demonstration of perpendicular baseline change with position of the scatterer. Perpendicular baseline and incidence angle change slightly with range and height.

Many interferometric processors utilize the normal baseline model in phase-to-height conversion. While this is our starting point in this toolbox as well, we aim to study any potential limitations and assess whether using a more realistic model is warranted and feasible. See Figure 4.3 for an illustration of this issue.

Algorithm 6 Phase to Height Conversion Algorithm

```
1: procedure PHASE TO HEIGHT CONVERSION
2:    $I \leftarrow$  Unrapped interferogram
3:    $B_{\perp} \leftarrow$  Perpendicular Baseline
4:    $\lambda \leftarrow$  Wavelength
5:    $\theta_i \leftarrow$  Incidence Angle
6:    $R \leftarrow$  Range
7:    $H \leftarrow$  Height Map
8:    $H = \text{heightconverter}(I, \lambda, B_{\perp}, \theta_i, R)$ 
   return  $U$ .
9: end procedure
```

4.2.2 SAR Interferometry Toolbox GUI

For ease of use, a graphical user interface was designed for ASELSAN SAR Interferometry Toolbox. The configuration of GUI can be seen in Figure 4.4. A user can perform fundamental SAR Interferometry operations by loading system parameters using corresponding buttons.

4.2.3 Toolbox Outputs

This toolbox is capable of performing the fundamental steps of interferometric SAR processing. Even though the main aim is to get a 3-D elevation map of the area of interested, intermediary products can be useful as well. Here, we define three main products of this process.

The first one is the wrapped interferogram of the scene. An example wrapped interferogram generated by the SAR Interferometry Toolbox is shown in Figure 4.13. Master image is demonstrated in Figure 4.5. The only system parameter provided with the data set is height of ambiguity of the system.

Second, the coherence map of the scene is presented as another product. Coherence maps can provide valuable information about scatterers in the scene [3] [24]. In Figure 4.7, a sample coherence map is given. Again, the DLR dataset was used

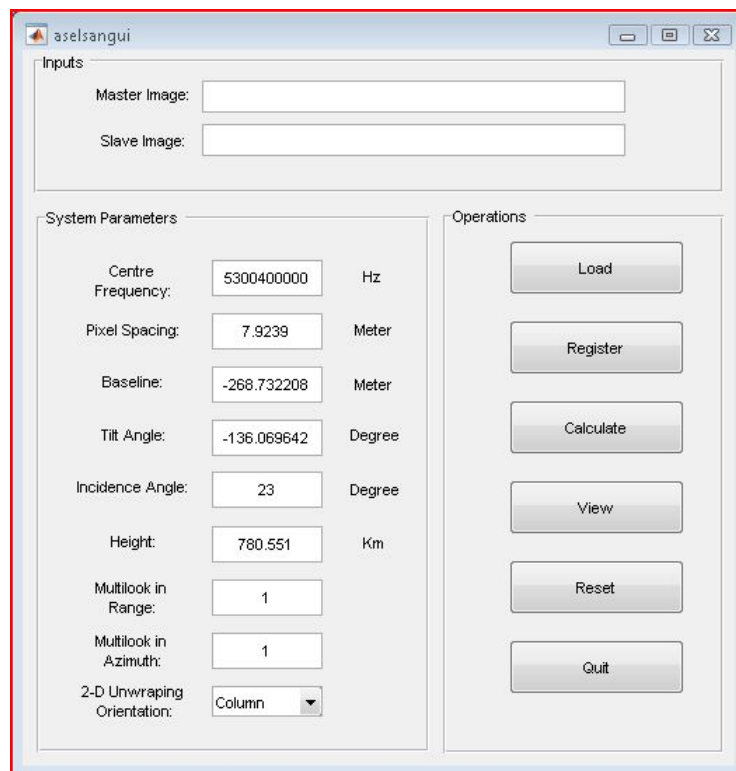


Figure 4.4: Graphical User Interface of SAR Interferometry Toolbox.

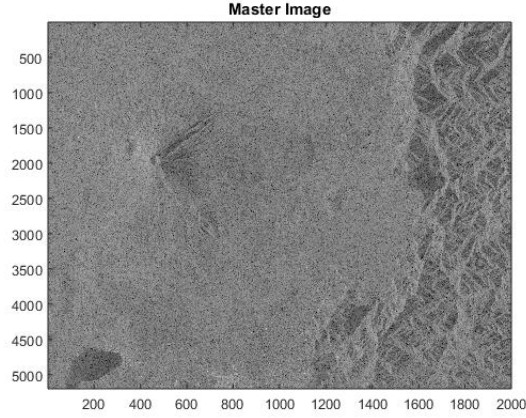


Figure 4.5: Master image of DLR dataset.

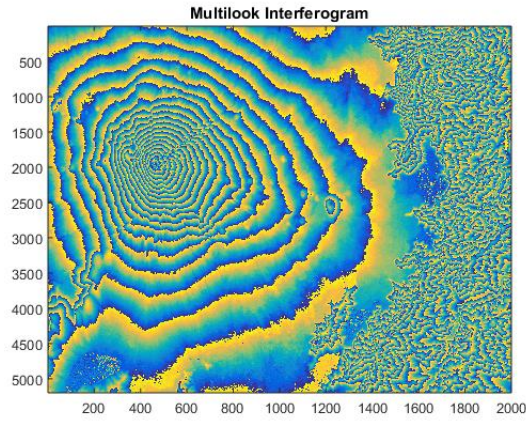


Figure 4.6: A flattened interferogram example produced by the SAR Interferometry Toolbox. All processing steps except flat earth calculation for this data is performed by the SAR Interferometry Toolbox. Each cycle corresponds to 167.89 meter height change.

to produce this coherence map.

As the end product of processing, a 3-D elevation map is delivered to users. The elevation map given in Figure 4.8 is generated from from the DLR dataset by the SAR Interferometry Toolbox. This appears to be a reasonable initial result.

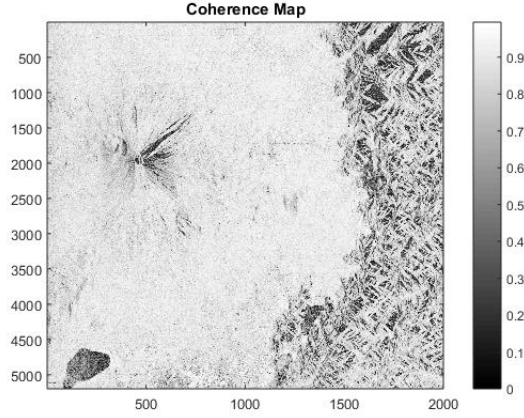


Figure 4.7: A coherence map example produced by the SAR Interferometry Toolbox.

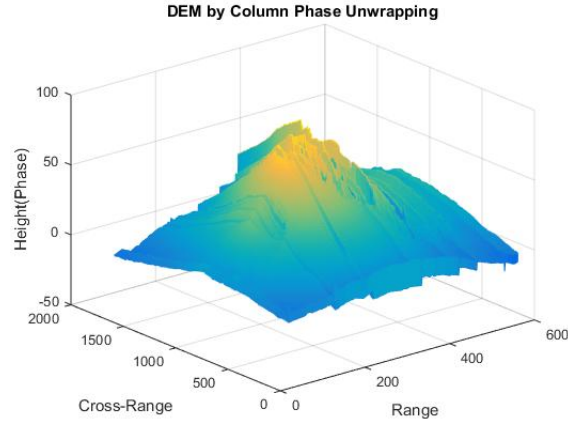


Figure 4.8: A digital elevation map produced from DLR dataset. All interferometric steps are performed by SAR Interferometry Toolbox Height of ambiguity is 167.89 m/cycle.

4.2.4 Tests and Analyses

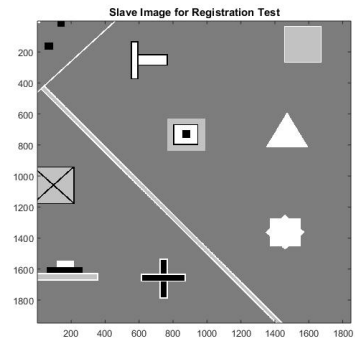
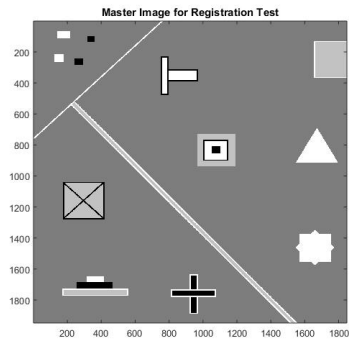
Image Registration

Image registration is an important step for SAR Interferometry processing. The accuracy of the image registration algorithm has a direct effect on relative phase preservation. Consequently, the image registration algorithm implemented in SAR

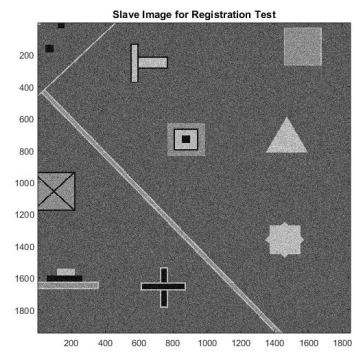
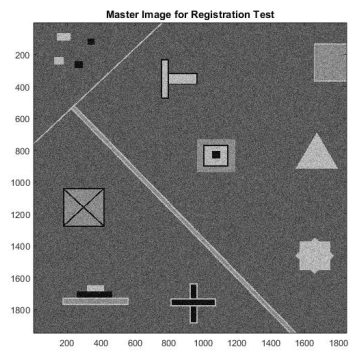
Interferometry Toolbox has been tested for different scenarios.

Test scenes which we used in our experiments can be seen in Figure 4.9. We create a synthetic scene that contains some distinct features which image registration algorithms can use. We carried out our tests over two different version of this scene, a noise free versions and a noisy version with an SNR of 0 dB. When images were exposed to higher noise levels, it becomes very hard to select features in the images. Therefore the images with 0 dB SNR's were used for testing procedure. Master and Slave images are shifted by 200 pixels in the horizontal direction and by 100 pixels in the vertical direction relative to each other.

Our purpose is to measure the accuracy of our image registration algorithm in estimating the relative shifts between the master and slave images. In this version of the toolbox, we limit the scope of the registration process to translations only, and do not consider other rigid registration problems involving rotation or scaling, as well as non-rigid registration problems involving, e.g., skewing or stretching.



(a) Synthetic Master Image, no noise is added (b) Synthetic Slave Image, no noise is added



(c) Synthetic Master Image, SNR=0 dB (d) Synthetic Slave Image, SNR=0 dB

Figure 4.9: Synthetic SAR Images for the Image Registration Test.

Our test procedure basically checks the robustness of the algorithm to human mistakes and noise. The algorithm needs human involvement. The user should select several regions of interest from both master and slave images which show high similarity. However, the user may not be as precise as he or she should be during this selection. Thus, we have investigated how much the algorithm is immune to human error. Table 4.2 and 4.3 show the result we have obtained from our test procedures. The test procedure we have followed for the first table is as follows. During the selection of control points, we assume that the user makes the specified amount of error while selecting control points in master and slave images. Suppose the user has to select two pairs. We assume that the user makes the same amount of error for the first pair and the second pair. For instance, the scenario that the user makes a 1 pixel error in X dimension for both of the pairs fits the procedure given in the first table. For the second table, we assume that the user selects one of the pairs perfectly, and makes an error for the other pair. The amounts of the selection error in terms of pixels are given in the table.

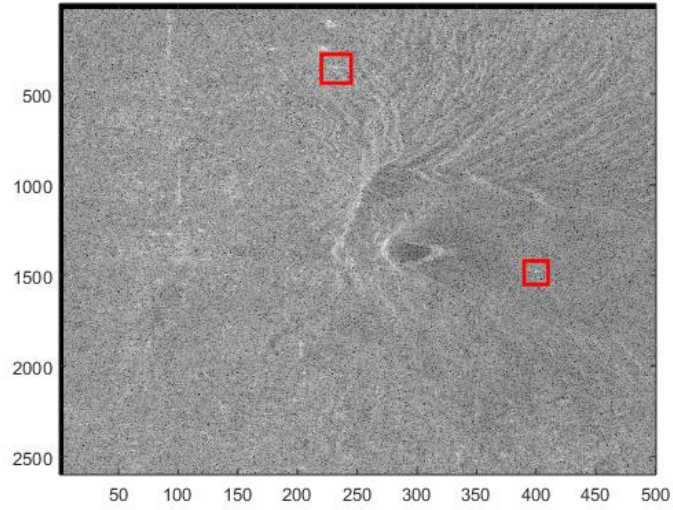
We also tested our method on real data. For this task, the Mount Vesuvius dataset was used. Since the images provided in this dataset are co-registered, we have intentionally created a shift between those images. Then, we have applied the same procedure previously used for the synthetic data tests. The results are presented in Tables 4.4 and 4.5. When we interpret the results of the registration tests, we can easily state that the registration algorithm works as expected. Unless the user selects some control points from outside of autocorrelation window used in the registration algorithm, it is expected that the registration algorithm we implemented would produce satisfactory results.

Data Type	ΔX_{err}	ΔY_{err}	$\hat{\Delta X}$	$\hat{\Delta Y}$
$\Delta X = 200\text{ px}$ $\Delta Y = 100\text{ px}$ No noise	1 px	0 px	200 px	100 px
	5 px	0 px	200 px	100 px
	10 px	0 px	200 px	100 px
	1 px	1 px	200 px	100 px
	5 px	5 px	200 px	100 px
	10 px	10 px	200 px	100 px
$\Delta X = 200\text{ px}$ $\Delta Y = 100\text{ px}$ 0 dB noise	1 px	0 px	200 px	100 px
	5 px	0 px	200 px	100 px
	10 px	0 px	200 px	100 px
	1 px	1 px	200 px	100 px
	5 px	5 px	200 px	100 px
	10 px	10 px	200 px	100 px

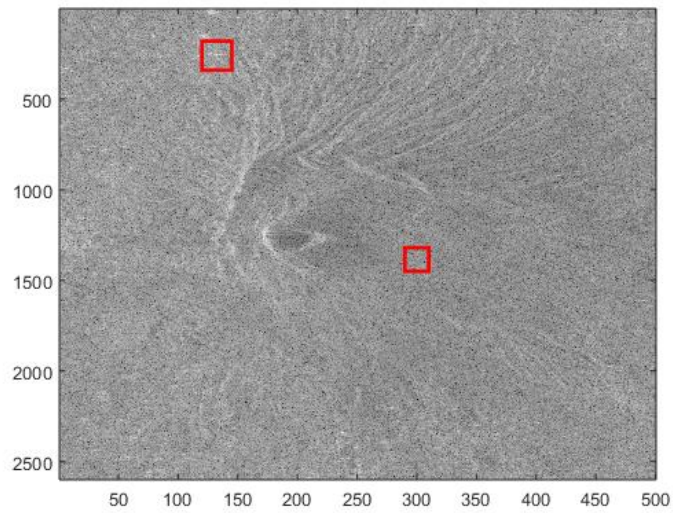
Table 4.2: Registration Test Results for Synthetic SAR dataset shown in Figure 4.9. The test procedure is as follows. We assume that the user makes the specified amount of error while selecting control points in master and slave image. Suppose the user has to select two pair, it is assumed that the user makes the same amount of error while selecting both pairs. Here, we present the amount of shift between images which the registration algorithm calculated. The amount of shifts between input master and slave images in X and Y dimension are denoted by ΔX and ΔY , respectively. ΔX_{err} and ΔY_{err} represent the selection errors between the control points in master and slave images in X and Y dimensions, respectively.

Data Type	ΔX_{err1}	ΔX_{err2}	ΔY_{err1}	ΔY_{err2}	$\hat{\Delta X}$	$\hat{\Delta Y}$
$\Delta X = 200\text{ px}$ $\Delta Y = 100\text{ px}$ No noise	1 px	0 px	0 px	0 px	200 px	100 px
	5 px	0 px	0 px	0 px	200 px	100 px
	10 px	0 px	0 px	0 p	200 px	100 px
	0 px	1 px	0 px	0 px	200 px	100 px
	0 px	5 px	0 px	0 px	200 px	100 px
	0 px	10 px	0 px	0 px	200 px	100 px
	1 px	1 px	0 px	0 px	200 px	100 px
	5 px	5 px	0 px	0 px	200 px	100 px
	10 px	10 px	0 px	0 px	200 px	100 px
$\Delta X = 200\text{ px}$ $\Delta Y = 100\text{ px}$ 0 dB Noise	1 px	0 px	0 px	0 px	200 px	100 px
	5 px	0 px	0 px	0 px	200 px	100 px
	10 px	0 px	0 px	0 px	200 px	100 px
	0 px	1 px	0 px	0 px	200 px	100 px
	0 px	5 px	0 px	0 px	200 px	100 px
	0 px	10 px	0 px	0 px	200 px	100 px
	1 px	1 px	0 px	0 px	200 px	100 px
	5 px	5 px	0 px	0 px	200 px	100 px
	10 px	10 px	0 px	0 px	200 px	100 px

Table 4.3: Registration Test Results for Synthetic SAR dataset shown in Figure 4.9. The test procedure is as follows. As previous test procedure described in Figure 4.2, we assume that the user makes the specified amount of error while selecting control points in master and slave image. However, the user selects one of the pairs perfectly in this time, and makes error for the other pair. The amount of the selection error in terms of pixel are defined in the table. Here, we present the amount of shift between images which the registration algorithm calculated. The amount of shifts between input master and slave images in X and Y dimension are denoted by ΔX and ΔY , respectively. ΔX_{err1} and ΔX_{err2} are the selection errors between the first and second control pair in master and slave images in X, respectively. ΔY_{err1} and ΔY_{err2} represent the same type error for Y dimension.



(a) Shifted Mount Vesuvius Master Image



(b) Shifted Mount Vesuvius Slave Image

Figure 4.10: Mount Vesuvius Data for the the registration test. The control points are pointed out with red squares.

Data Type	ΔX_{err}	ΔY_{err}	$\hat{\Delta X}$	$\hat{\Delta Y}$
ΔX 100 px ΔY 100 px	1 px	0 px	100 px	100 px
	5 px	0 px	100 px	100 px
	10 px	0 px	100 px	100 px
	1 px	1 px	100 px	100 px
	5 px	5 px	100 px	100 px
	10 px	10 px	100 px	100 px

Table 4.4: Registration Test Results for the Mount Vesuvius dataset shown in Figure 4.10. The test procedure is as follows. We assume that the user makes the specified amounts of error while selecting control points in master and slave images. Suppose the user has to select two pairs of control points. It is assumed that the user makes the same amount of error while selecting both pairs. Here, we present the amount of shift between images which the registration algorithm calculated. The amounts of shift between input master and slave images in X and Y dimension are denoted by ΔX and ΔY , respectively. ΔX_{err} and ΔY_{err} represents the selection errors between the control points in master and slave images in X and Y dimensions, respectively.

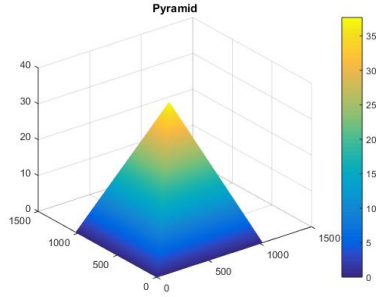
Complex Multilooking and 2-D Phase Unwrapping

Complex multilooking and 2-D phase unwrapping are the other steps that affect the preservation of the interferometric phase. We tried to measure the performance of these steps with respect to different system parameters and different scenarios.

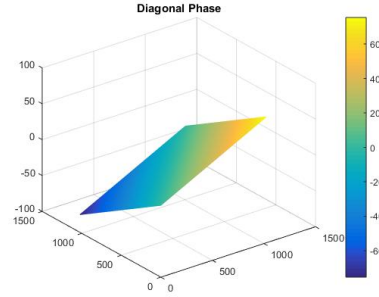
First of all, we created different height profiles in order to test our system for different land shapes. These profiles are pyramid, diagonal plane, sheared planes, parabolic surface and cut pyramid. They can be seen in Figure 4.11.

Data Type	ΔX_{err1}	ΔX_{err2}	ΔY_{err1}	ΔY_{err2}	$\hat{\Delta X}$	$\hat{\Delta Y}$
ΔX 100 px ΔY 100 px	1 px	0 px	0 px	0 px	100 px	100 px
	5 px	0 px	0 px	0 px	100 px	100 px
	10 px	0 px	0 px	0 p	100 px	100 px
	0 px	1 px	0 px	0 px	100 px	100 px
	0 px	5 px	0 px	0 px	100 px	100 px
	0 px	10 px	0 px	0 px	100 px	100 px
	1 px	1 px	0 px	0 px	100 px	100 px
	5 px	5 px	0 px	0 px	100 px	100 px
	10 px	10 px	0 px	0 px	100 px	100 px

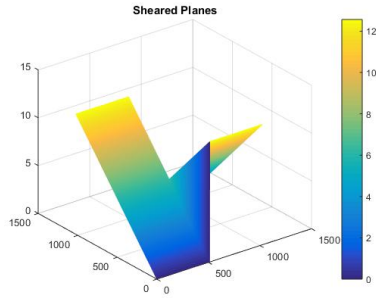
Table 4.5: Registration Test Results for Mount Vesuvius dataset shown in Figure 4.10. The test procedure is as follows. As in the previous test procedure described in Figure 4.2, we assume that the user makes the specified amount of error while selecting control points in master and slave images. However, the user selects one of the pairs perfectly this time, and makes an error for the other pair. The amount of the selection error in terms of pixels are given in the table. Here, we present the amount of shift between images which the registration algorithm calculated. The amounts of shift between input master and slave images in X and Y dimension are denoted by ΔX and ΔY , respectively. ΔX_{err1} and ΔX_{err2} are the selection errors in X between the master and slave images, in the first and the second control pairs, respectively. ΔY_{err1} and ΔY_{err2} represent the same type error in the Y dimension.



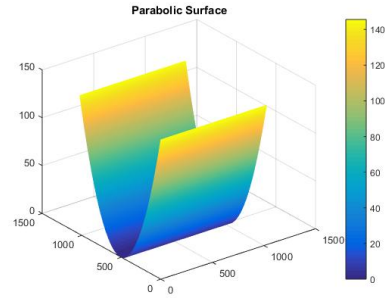
(a) Pyramid



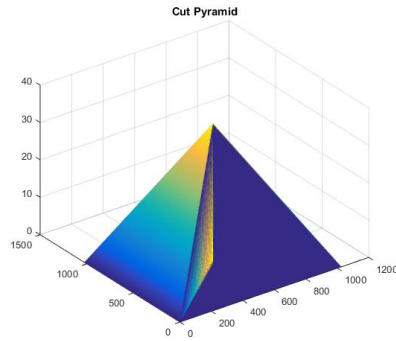
(b) Diagonal Plane



(c) Sheared Planes



(d) Parabolic Surface



(e) Cut Pyramid

Figure 4.11: Synthetic Phase Profiles. Here, the five profiles used for 2-D phase unwrapping test operation are presented. These are pyramid, diagonal plane, sheared planes, parabolic surface, and cut pyramid.

Test data were created by doing phase wrapping operation over the phase profiles shown in 4.11, and adding white Gaussian complex noise.

Here, we tested our algorithm in two different ways. First, the effect of multilooking window size on phase error was investigated. Then, the performance of the 2-D phase unwrapping algorithm was tested for different scenarios and parameters.

As it was pointed out in [3] [16], interferometric phase, relative phase in other terms, is calculated by the formula given by:

$$\varphi_{ML} = \angle \left(\sum_{n=1}^N u_1^* u_2 \right) \quad (4.6)$$

In fact, this is maximum likelihood (ML) estimation of the relative phase. In theory, this estimation should lead to a better phase value with increasing the size of the multilooking window and increasing coherence values, as it is depicted in Figure 4.12.

In the interest of validating this relation, we calculated some interferograms from noisy data with different multilooking window sizes. Several synthetic interferogram examples are shown in Figure 4.13 and 4.14.

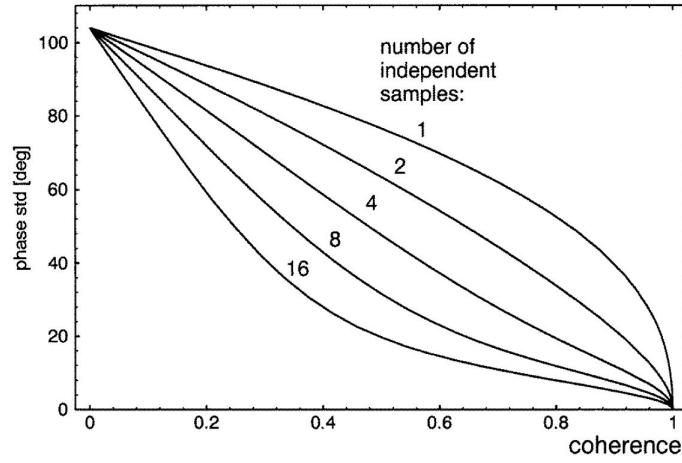
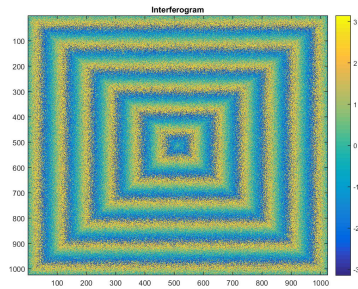
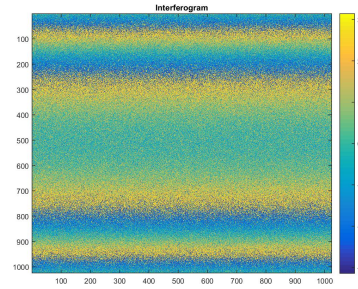


Figure 4.12: Standard deviation of the phase estimator given in Equation 4.6 with respect to multilooking and coherence. The image was taken from [3]



(a) Single look interferogram from pyramid phase profile with 0db SNR.



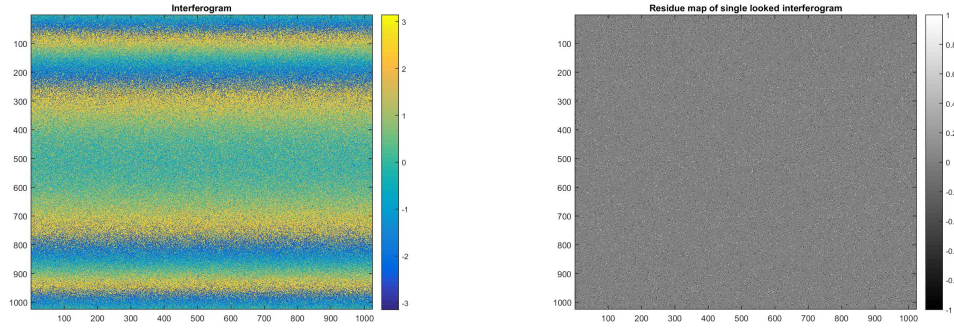
(b) Single look interferogram from parabolic plane phase profile with 0db SNR.

Figure 4.13: Synthetic Interferogram Examples.

In order to see the effect of the multilooking operation, we recreated those interferograms with different multilooking window sizes. After phase unwrapping, phase RMSE was calculated by using the unwrapped interferograms and the original phase profiles. RMSE values with respect to window sizes are presented in Figure 4.15. Also, height RMSE values are calculated for a system which has 100 meter height of ambiguity, and they are shown in Figure 4.16. In all scenarios, RMSE values decrease with the increasing size of the multilooking window. This result is consistent with Figure 4.12.

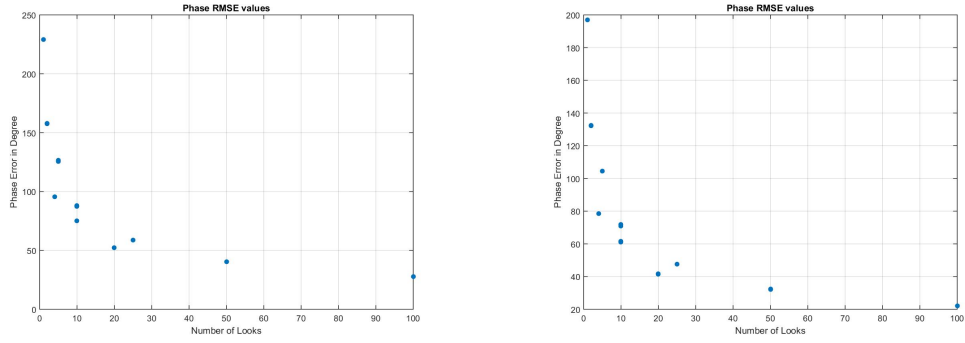
Another important step for the SAR Interferometry Process is 2-D phase unwrapping. In SAR Interferometry Toolbox v.1, a path dependent 2-D phase unwrapping method, Itoh's Method, was implemented. This method is quite sensitive to the phase inconsistencies in the data, i.e., residues. The presence of residues violate the path independence property of the interferograms. As an example to this phenomenon, the interferogram and residue map in Figure 4.14 can be analyzed. Evidently, the number of residues are proportional to the noise level. On the other hand, there are other factors which affect the presence of the residues, such as the layover effect.

Here, we tested how the multilooking operation make can the interferogram better for the 2-D phase unwrapping algorithm. In Figures 4.17, 4.18, and 4.19, unwrapped interferograms. They were created by using multilooking windows of different sizes.



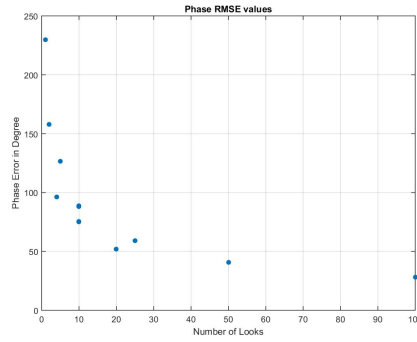
(a) Single look interferogram of parabolic (b) Residue map of single look interferogram.

Figure 4.14: A Single look interferogram and its residue map.



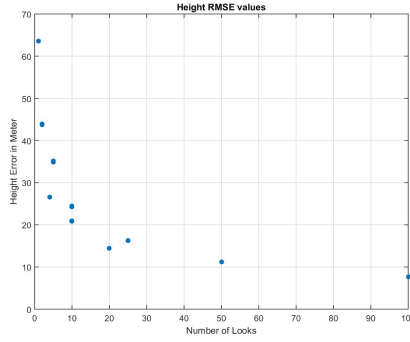
(a) Phase RMSE for Pyramid

(b) Phase RMSE for Parabolic Surface

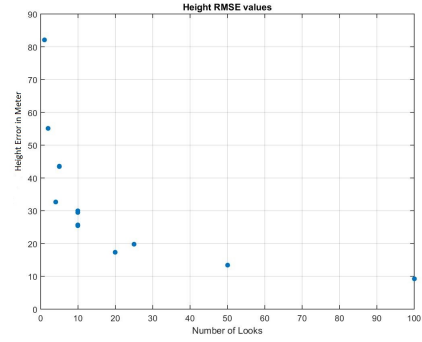


(c) Phase RMSE for Diagonal Plane

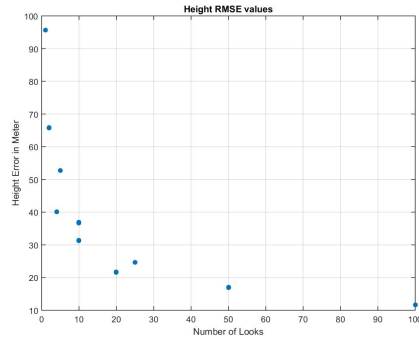
Figure 4.15: Phase RMSE's with respect to different multilooking parameters are presented. Each one of these graphs shows the RMSE in phase estimation for a different phase profile.



(a) Height RMSE for Pyramid

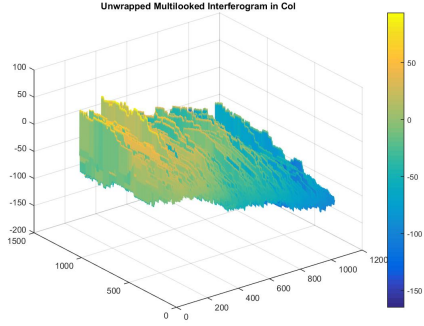


(b) Height RMSE for Parabolic Surface

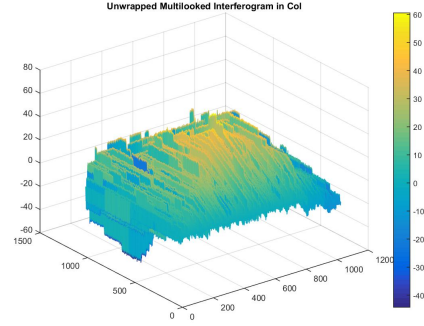


(c) Height RMSE for Diagonal Plane

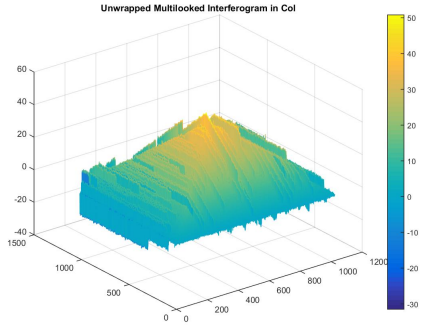
Figure 4.16: Height RMSE's with respect to different multilooking parameters for a system has height of ambiguity $h_{amb} = 100m$. Each one of these graphs are denotes the RMSE in height estimation for a different phase profile.



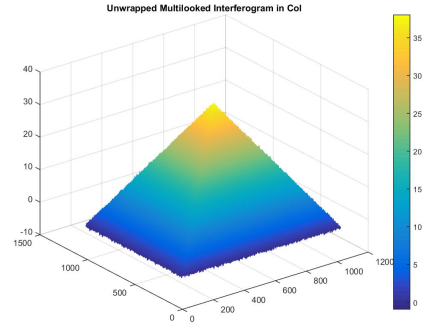
(a) For multilooking window size 1×1



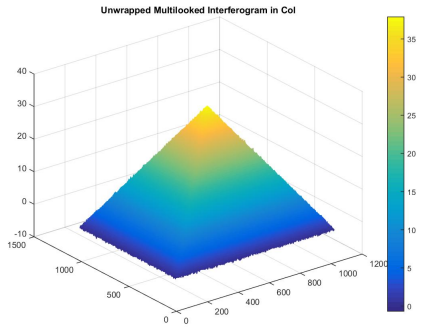
(b) For multilooking window size 1×2



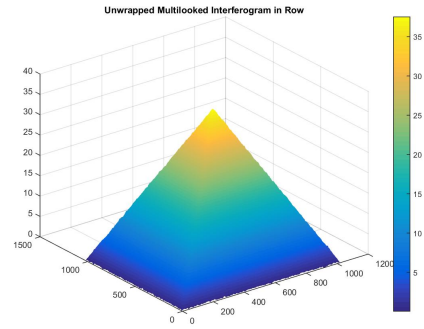
(c) For multilooking window size 1×5



(d) For multilooking window size 2×5

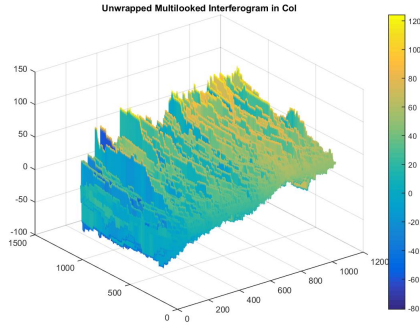


(e) For multilooking window size 5×5

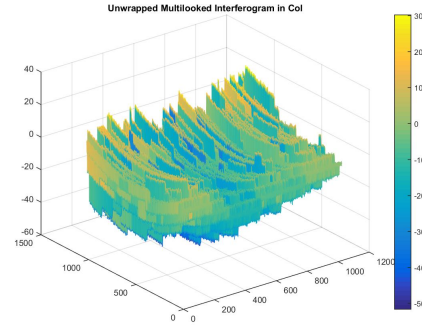


(f) For multilooking window size 10×10

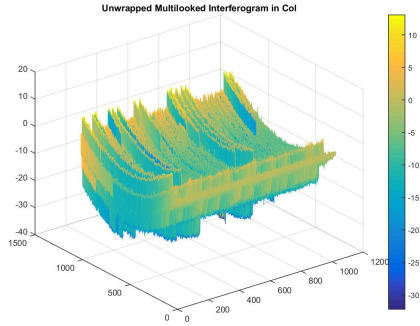
Figure 4.17: Unwrapped interferograms of pyramid. They are averaged with different multilooking windows. Clearly, we got better results with the increasing size of the multilooking window.



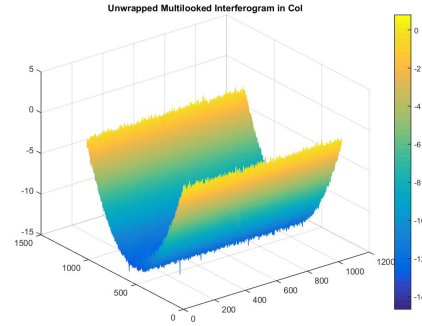
(a) For multilooking window size 1×1



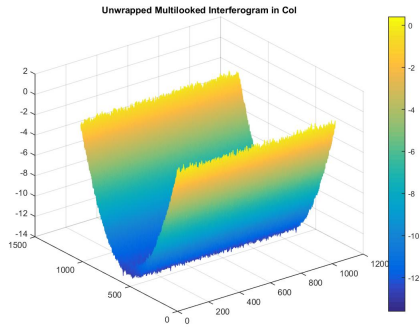
(b) For multilooking window size 1×2



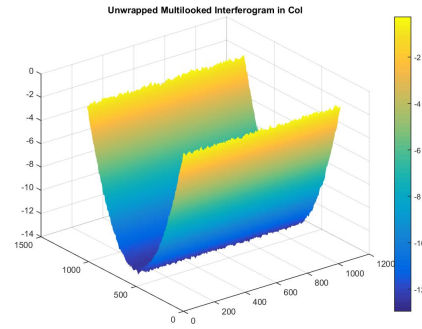
(c) For multilooking window size 1×5



(d) For multilooking window size 2×5

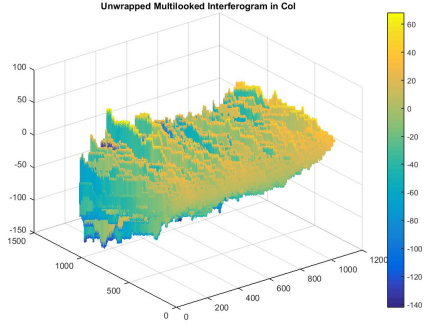


(e) For multilooking window size 5×5

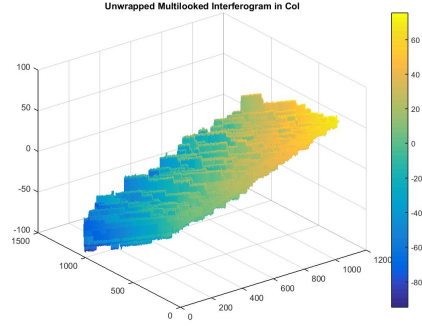


(f) For multilooking window size 10×10

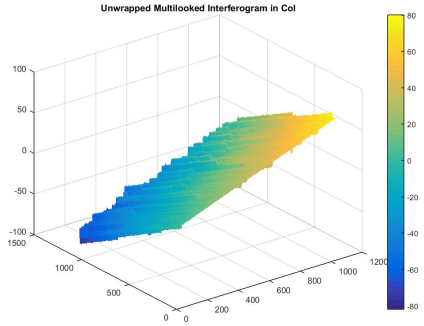
Figure 4.18: Unwrapped Interferograms of parabolic surface. They are averaged with different multilooking windows. Clearly, we got better results with the increasing size of the multilooking window.



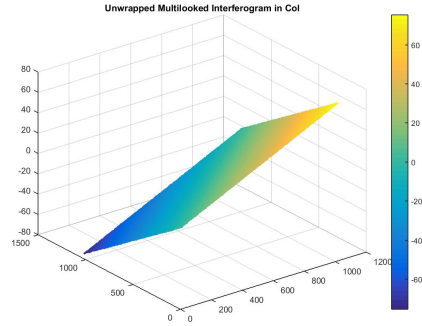
(a) For multilooking window size 1×1



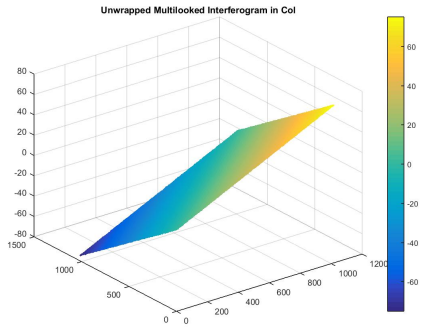
(b) For multilooking window size 1×2



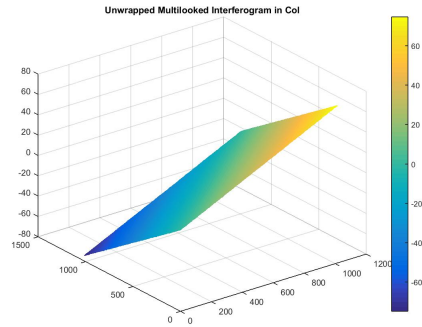
(c) For multilooking window size 1×5



(d) For multilooking window size 2×5



(e) For multilooking window size 5×5

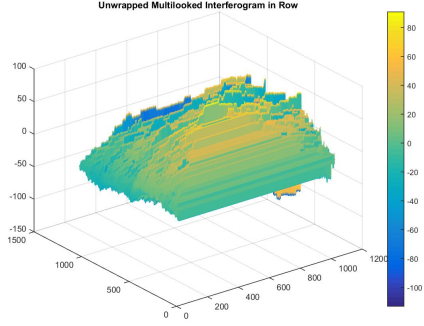


(f) For multilooking window size 10×10

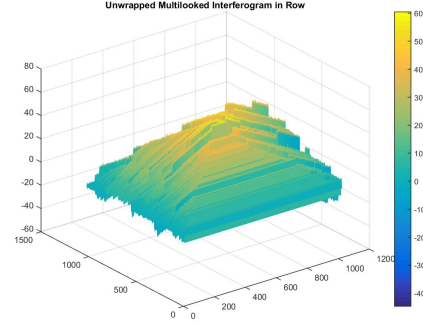
Figure 4.19: Unwrapped Interferograms of diagonal plane. They are averaged with different multilooking windows. Clearly, we got better results with the increasing size of the multilooking window.

On the other hand, there are height profiles that contains phase inconsistencies which multilooking operation cannot handle. Sharp and rapid phase changes may not be resolved by multilooking. In order to test this, we tested our algorithm on two different phase profiles, sheared planes and cut pyramid. Those profiles are depicted in Figure 4.11. Those profiles contain sharp phase transitions which are hard to unwrap.

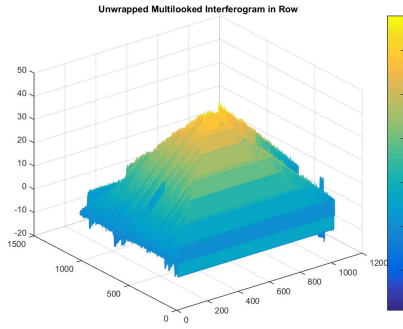
We tried to unwrap those phase profiles with our 2-D phase unwrapping algorithm. The results are provided in Figures 4.20 and 4.21. The regions which are incorrectly unwrapped can be seen easily. A phase unwrapping error corresponds to a phase error at the scale of height of ambiguity which is on the order of tens of meter. This is much higher than an acceptable error range. Therefore, these regions which have potentially low phase stability are excluded from DEM and error analysis [11]. The implemented algorithm cannot exclude the areas which show low phase stability, so the error analysis for this algorithm may not be informative about the performance. Here, we tried to show that the implemented algorithm is capable of doing the unwrapping operation successfully in certain cases.



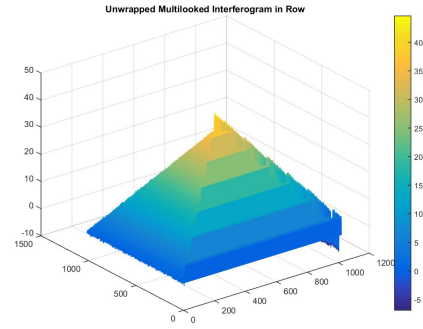
(a) For multilooking window size 1×1



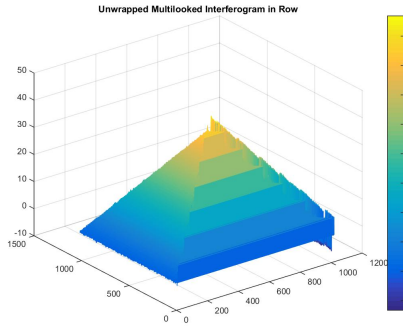
(b) For multilooking window size 1×2



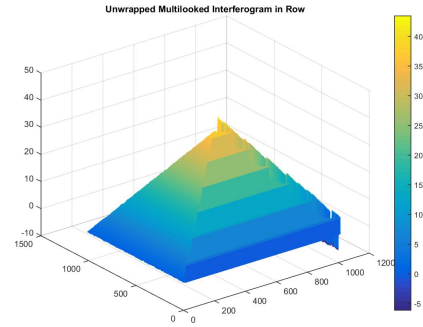
(c) For multilooking window size 1×5



(d) For multilooking window size 2×5

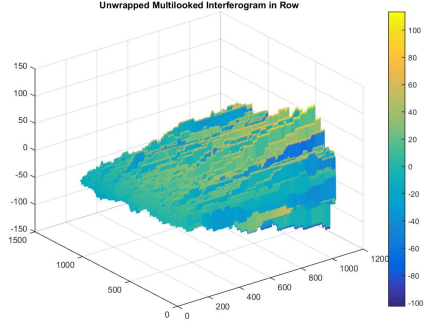


(e) For multilooking window size 5×5

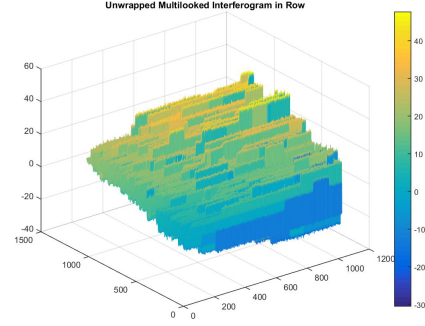


(f) For multilooking window size 10×10

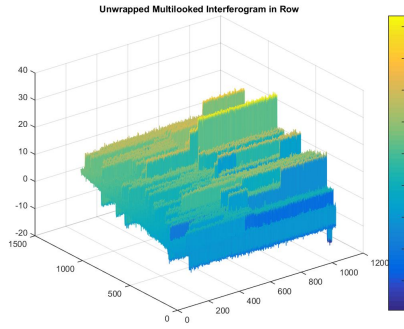
Figure 4.20: Unwrapped interferograms of cut pyramid plane. They are filtered with different multilooking windows.



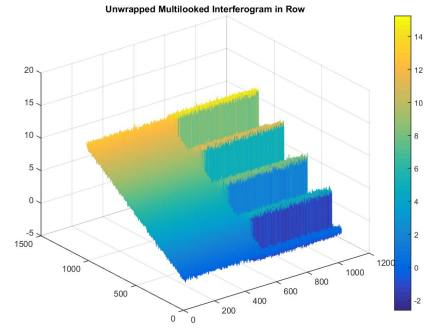
(a) For multilooking window size 1×1



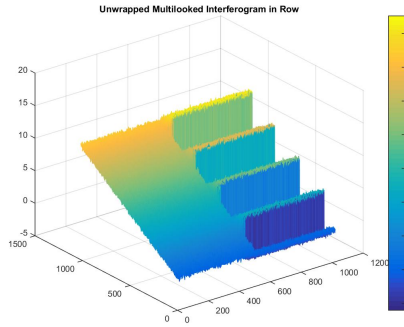
(b) For multilooking window size 1×2



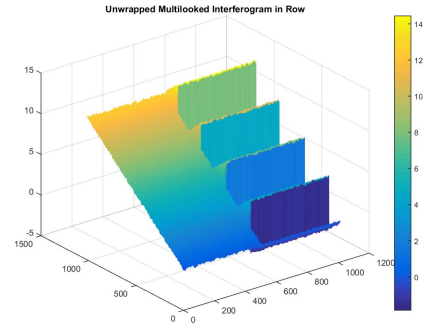
(c) For multilooking window size 1×5



(d) For multilooking window size 2×5



(e) For multilooking window size 5×5



(f) For multilooking window size 10×10

Figure 4.21: Unwrapped interferograms of sheared plane. They are filtered with different multilooking windows.

Even though we increase the size of the multilooking window, we could not get a satisfactory result. These sharp and quick phase transitions basically breaks the path independency of the interferograms. Therefore, the implemented 2-D phase unwrapping algorithm fails eventually.

In the real world, there are many factors that can cause low coherence or geometric distortions. For example, it is very likely to observe foreshortening or shadow effect in mountainous regions due to high slope. Eventually, the need of a better 2-D phase unwrapping algorithm emerges in order to increase the quality of DEMs.

Discussion

In this section, the outcomes which can be inferred from the test results are discussed.

By examining the results of the registration tests, we can say that our algorithm is fairly immune to human error. In our trials, we tried all human error combinations as much as we can, such as selecting one control pair correctly and selecting the other one with some pixel error. Unless the user error exceeds the size of the auto-correlation window, the registration algorithm can tolerate this kind of mistakes. On the other hand, the real data may contain different distortions, and these distortions may decrease the performance of the registration algorithm, eventually.

Clearly, we got better results with the increasing size of the multilooking window. The increasing size of the multilooking window increased the accuracy of relative phase estimates. However, this smoothing causes a resolution loss as well. If the scene contains sharp transitions, like rough mountains, then we may lose the relevant phase information for rough surfaces. Consequently, the size of the multilooking window is a parameter which should be adjusted based on the scene

properties and system parameters.

Lastly, we evaluated the 2-D phase unwrapping algorithm. Previously, we mentioned that the algorithm which we implemented is a path-dependent phase unwrapping algorithm. As a consequence, we showed that any phase inconsistency, i.e., residue, can create a phase unwrapping error. In the real world, there are many factors which create such phase residues in the data. For example, coherence loss due to large time delays between acquisitions and sharp transitions in the scene can cause that. Even though, our method produces good results for some scenarios, a better phase unwrapping algorithm is a must for SAR Interferometry processing with real data.

Chapter 5

Conclusion

5.1 Summary

In this thesis, we have proposed two tools for SAR Interferometry processing. First, SDCIA was presented as a new image enhancement method to solve the autofocus problem and preservation of relative phase between interferometric channels. Secondly, we have developed the SAR Interferometry Toolbox for fundamental SAR Interferometry processing.

As we stated, Sparsity-driven Coupled Imaging and Autofocusing for Interferometric SAR (SDCIA) is a joint image enhancement and reconstruction algorithm. In comparison to the existing image reconstruction algorithms, it enhances the first and second SAR images jointly to preserve the relative phase information between the first and second acquisitions, and it handles the autofocus problem to eliminate the effect of platform motion errors at the same time. To show the effectiveness of our method, we have performed preliminary tests on synthetic SAR data. In addition, we compared it with existing methods, Sparsity-driven Autofocus by Önhon and Çetin [20] and Joint Enhancement by Dual Descent by Ramakrishnan et al. [23]. Based on the results we got, we discussed the pros and

cons of SDCIA.

As the second tool, we produced the SAR Interferometry Toolbox within the content of the ASELSAN SAR Interferometry Project. SAR Interferometry Toolbox is a software processor for SAR Interferometry. It is capable of performing the fundamental steps for IfSAR which are registration, interferogram generation, 2-D phase unwrapping, and phase-to-height conversion. The contents of these steps are explained in a detailed way, and their performances are demonstrated with the presented test results.

5.2 Potential Research Directions

The work performed in this thesis can be extended in several directions, which we discuss briefly in subsequent subsections.

5.2.1 Testing SDCIA on a real world scenario

In our trials, the performance of SDCIA was assessed only on synthetic scenes. It has been demonstrated that SDCIA has some advantages over existing methods. Testing SDCIA on real datasets would be a natural next step of this research. Testing our method on more realistic data may reveal more detailed information about the capabilities of SDCIA.

5.2.2 Extension of SDCIA to more than two channels

In this study, we have tested the performance of SDCIA when there are two interferometric image acquisitions. In the remote sensing literature, there are image modalities which needs more than two image acquisitions. One of these image modalities is Differential Interferometric SAR (DINSAR). The main aim of this

image modality is to measure the changes on the Earth’s surface. Our approach can in principle be applied over the images used in Differential IfSAR.

Another image modality for which SDCIA can be useful is Tomographic SAR (TomoSAR). A 3-D model of the scene with high resolution would be obtained as the result of TomoSAR processing. TomoSAR needs more than two images of the scene. Therefore, when SDCIA is used in the context of TomoSAR processing, the precision of the 3-D model constructed by TomoSAR may increase.

5.2.3 Application of the Proposed Method to other domains

Our method can be adapted to multichannel imaging modalities other than SAR and application domains other than remote sensing of the earth. For example, SDCIA can be used in multichannel medical imaging modalities. Motion errors are a serious problem for medical images as well. During the imaging procedure, patients can move unintentionally, or the images may degrade due to constant motion of heart beats. SDCIA can be a solution to produce higher quality images.

Appendix A

In this appendix, we describe how we get from Eqn. (3.7) to Eqn. (3.8). The cost function in (3.7) for phase error estimation is as follows:

$$\Delta\phi_{1m}^{(n+1)} = \underset{\Delta\phi_{1m}}{\operatorname{argmin}} L(f_1^{(n+1)}, \Delta\phi_{1m}) \quad (\text{A.1})$$

$$\Delta\phi_{2m}^{(n+1)} = \underset{\Delta\phi_{2m}}{\operatorname{argmin}} L(f_2^{(n+1)}, \Delta\phi_{2m}) \quad (\text{A.2})$$

These equations can be rewritten as follows:

$$\Delta\phi_{1m}^{(n+1)} = \underset{\Delta\phi_1}{\operatorname{argmin}} \left\| g_{1m} - \exp(j\Delta\phi_1) C_{1m}(\phi_1^{(n)}) f_1^{(n+1)} \right\|_2^2 \quad (\text{A.3})$$

$$\Delta\phi_{2m}^{(n+1)} = \underset{\Delta\phi_2}{\operatorname{argmin}} \left\| g_{2m} - \exp(j\Delta\phi_2) C_{2m}(\phi_2^{(n)}) f_2^{(n+1)} \right\|_2^2 \quad (\text{A.4})$$

where $\Delta\phi_{1m}^{(n+1)}$ and $\Delta\phi_{2m}^{(n+1)}$ are the phase error estimates at iteration $n + 1$ corresponding to the m^{th} aperture position of the first and second acquisitions, respectively. Similarly, g_{1m} , g_{2m} , $C_{1m}(\phi^{(n)})$, $C_{2m}(\phi^{(n)})$ are the parts of the collected data and observation matrix which are related to the m^{th} position of the first and second acquisitions.

If we evaluate the norm term in the cost function, we get the following expression. For simplicity, we will do it for only single acquisitions case.

$$\|g_m - e^{j\Delta\phi} C_m(\phi^{(n)}) f^{(n+1)}\|_2^2 = (g_m - e^{j\Delta\phi} C_m(\phi^{(n)}) f^{(n+1)})^H (g_m - e^{j\Delta\phi} C_m(\phi^{(n)}) f^{(n+1)})$$

$$\begin{aligned} &= g_m^H g_m - g_m^H e^{(j\phi_{1D}(m))} C_m f^{(n+1)} - f^{(n+1)H} \overbrace{C_m^H (e^{(j\phi_{1D}(m))})^H}^{e^{(-j\phi_{1D}(m))}} g_m + \\ &\quad f^{(n+1)H} \overbrace{C_m^H (e^{(j\phi_{1D}(m))})^H}^{e^{(-j\phi_{1D}(m))}} e^{(j\phi_{1D}(m))} C_m f^{(n+1)} \end{aligned}$$

If we evaluate the norm expression, we will get the following.

$$\begin{aligned} &= g_m^H g_m - g_m^H [\cos(\phi_{1D}(m)) + j \sin(\phi_{1D}(m))] C_m f^{(n+1)} - \\ &\quad f^{(n+1)H} C_m^H [\cos(\phi_{1D}(m)) - j \sin(\phi_{1D}(m))] g_m + f^{(n+1)H} C_m^H C_m f^{(n+1)} \\ &= g_m^H g_m - 2\Re\{\cos(\phi_{1D}(m)) f^{(n+1)H} C_m^H g_m\} + 2\Re\{j \sin(\phi_{1D}(m)) f^{(n+1)H} C_m^H g_m\} + \\ &\quad f^{(n+1)H} C_m^H C_m f^{(n+1)} \\ &= g_m^H g_m - 2\cos(\phi_{1D}(m)) \Re\{f^{(n+1)H} C_m^H g_m\} + 2\sin(\phi_{1D}(m)) \Im\{f^{(n+1)H} C_m^H g_m\} + \\ &\quad f^{(n+1)H} C_m^H C_m f^{(n+1)} \end{aligned}$$

$$\text{Let } \Re\{f^{(n+1)H} C_m^H g_m\} = \Re, \text{ and } \Im\{f^{(n+1)H} C_m^H g_m\} = \Im$$

Since we can write $\sin(\phi_{1D}(m))$ as $\cos(\phi_{1D}(m) - \frac{\pi}{2})$, the equation becomes

$$\begin{aligned} \|g_m - e^{j\Delta\phi} C_m(\phi^{(n)}) f^{(n+1)}\|_2^2 = g_m^H g_m - 2[\Re \cos(\phi_{1D}(m)) + \Im \cos(\phi_{1D}(m) - \frac{\pi}{2})] + \\ f^{(n+1)H} C_m^H C_m f^{(n+1)} \end{aligned}$$

The cosines in the previous equation can be added with phasor addition rule to a single cosine. The phasors for the terms $\Re \cos(\phi_{1D}(m))$ and $\Im \cos(\phi_{1D}(m) - \frac{\pi}{2})$ can be seen below.

$$P_1 = \Re e^{j0} = \Re \quad P_2 = \Im e^{-\frac{j\pi}{2}} = -j\Im$$

If we add them, we get

$$P_1 + P_2 = \Re + (-j\Im) = \Re - j\Im$$

The magnitude and phase of final phasor can be calculated as follows.

$$magnitude = \sqrt{\Re^2 + \Im^2} \quad phase = \arctan(\frac{-\Im}{\Re})$$

As final result, we would get the following equation.

$$\begin{aligned} \|g_m - e^{j\Delta\phi} C_m(\phi^{(n)}) f^{(n+1)}\|_2^2 = g_m^H g_m - 2\sqrt{\Re^2 + \Im^2} \cos[\phi_{1D}(m) + \arctan(\frac{-\Im}{\Re})] + \\ f^{(n+1)H} C_m^H C_m f^{(n+1)} \end{aligned}$$

Bibliography

- [1] Digital terrain elevation data [dted], 2000.
- [2] Richard Bamler and Michael Eineder. Scansar processing using standard high precision sar algorithms. *Geoscience and Remote Sensing, IEEE Transactions on*, 34(1):212–218, 1996.
- [3] Richard Bamler and Philipp Hartl. Synthetic aperture radar interferometry. *Inverse problems*, 14(4):R1, 1998.
- [4] DP Belcher and CJ Baker. High resolution processing of hybrid strip-map/spotlight mode sar. In *Radar, Sonar and Navigation, IEE Proceedings*-, volume 143, pages 366–374. IET, 1996.
- [5] Paolo Berardino, Gianfranco Fornaro, Riccardo Lanari, and Eugenio Sansosti. A new algorithm for surface deformation monitoring based on small baseline differential sar interferograms. *IEEE Transactions on Geoscience and Remote Sensing*, 40(11):2375–2383, 2002.
- [6] Thomas Blumensath and Mike E Davies. Iterative hard thresholding for compressed sensing. *Applied and computational harmonic analysis*, 27(3):265–274, 2009.
- [7] Alan C Bovik. *Handbook of image and video processing*. Academic press, 2010.

- [8] Müjdat Çetin and William Clement Karl. Feature-enhanced synthetic aperture radar image formation based on nonquadratic regularization. *IEEE Transactions on Image Processing*, 10(4):623–631, 2001.
- [9] Mario Costantini. A novel phase unwrapping method based on network programming. *Geoscience and Remote Sensing, IEEE Transactions on*, 36(3):813–821, 1998.
- [10] Alessandro Ferretti, Andrea Monti-Guarnieri, Claudio Prati, Fabio Rocca, and Didier Massonet. *InSAR Principles-Guidelines for SAR Interferometry Processing and Interpretation*, volume 19. 2007.
- [11] Dennis C Ghiglia and Mark D Pritt. *Two-dimensional phase unwrapping: theory, algorithms, and software*, volume 4. Wiley New York, 1998.
- [12] Dennis C Ghiglia and Louis A Romero. Robust two-dimensional weighted and unweighted phase unwrapping that uses fast transforms and iterative methods. *JOSA A*, 11(1):107–117, 1994.
- [13] Charles VJ Jakowatz, Daniel E Wahl, Paul H Eichel, Dennis C Ghiglia, and Paul A Thompson. *Spotlight-Mode Synthetic Aperture Radar: A Signal Processing Approach: A Signal Processing Approach*. Springer Science & Business Media, 2012.
- [14] Gerhard Krieger, Alberto Moreira, Hauke Fiedler, Irena Hajnsek, Marian Werner, Marwan Younis, and Manfred Zink. TanDEM-X: a satellite formation for high-resolution sar interferometry. *IEEE Transactions on Geoscience and Remote Sensing*, 45(11):3317–3341, 2007.
- [15] Remco Kroes, Oliver Montenbruck, William Bertiger, and Pieter Visser. Precise grace baseline determination using gps. *GPS Solutions*, 9(1):21–31, 2005.

- [16] Jong-Sen Lee, Karl W Hoppel, Stephen A Mango, and Allen R Miller. Intensity and phase statistics of multilook polarimetric and interferometric sar imagery. *IEEE Transactions on Geoscience and Remote Sensing*, 32(5):1017–1028, 1994.
- [17] Alberto Moreira, Gerhard Krieger, Hauke Fiedler, Irena Hajnsek, Marwan Younis, Manfred Zink, and Marian Werner. Advanced interferometric sar techniques with tandem-x. In *Radar Conference, 2008. RADAR'08. IEEE*, pages 1–5. IEEE, 2008.
- [18] Robert L Morrison, Minh N Do, and David C Munson. Mca: A multichannel approach to sar autofocus. *IEEE transactions on image processing*, 18(4):840–853, 2009.
- [19] F. Muirhead, B. Mulgrew, I.H. Woodhouse, and D. Greig. Sparsity-driven autofocus for multipass SAR tomography. In *SAR Image Analysis, Modeling, and Techniques XV*, volume 9642, page 96420G. International Society for Optics and Photonics, 2015.
- [20] N. Özben Önhon and Müjdat Çetin. A sparsity-driven approach for joint SAR imaging and phase error correction. *IEEE Transactions on Image Processing*, 21(4):2075–2088, 2012.
- [21] C Prati and F Rocca. Limits to the resolution of elevation maps from stereo SAR images. *Remote Sensing*, 11(12):2215–2235, 1990.
- [22] Bernhard Rabus, Michael Eineder, Achim Roth, and Richard Bamler. The shuttle radar topography mission—a new class of digital elevation models acquired by spaceborne radar. *ISPRS journal of photogrammetry and remote sensing*, 57(4):241–262, 2003.

- [23] Naveen Ramakrishnan, Emre Ertin, and Randolph L Moses. Enhancement of coupled multichannel images using sparsity constraints. *IEEE Transactions on Image Processing*, 19(8):2115–2126, 2010.
- [24] Paul A Rosen, Scott Hensley, Ian R Joughin, Fuk K Li, Soren N Madsen, Ernesto Rodriguez, and Richard M Goldstein. Synthetic aperture radar interferometry. *Proceedings of the IEEE*, 88(3):333–382, 2000.
- [25] MS Seymour and IG Cumming. Maximum likelihood estimation for sar interferometry. In *Geoscience and Remote Sensing Symposium, 1994. IGARSS'94. Surface and Atmospheric Remote Sensing: Technologies, Data Analysis and Interpretation., International*, volume 4, pages 2272–2275. IEEE, 1994.
- [26] Yun Shao, Xiangtao Fan, Hao Liu, Jianhua Xiao, S Ross, B1 Brisco, R Brown, and G Staples. Rice monitoring and production estimation using multitemporal radarsat. *Remote sensing of Environment*, 76(3):310–325, 2001.
- [27] David Small, Paolo Pasquali, and Stefan Fuglistaler. A comparison of phase to height conversion methods for sar interferometry. In *Geoscience and Remote Sensing Symposium, 1996. IGARSS'96. 'Remote Sensing for a Sustainable Future.', International*, volume 1, pages 342–344. IEEE, 1996.
- [28] D.E. Wahl, P.H. Eichel, D.C. Ghiglia, and C.V. Jakowatz. Phase gradient autofocus - a robust tool for high resolution SAR phase correction. *IEEE Transactions on Aerospace and Electronic Systems*, 30(3):827–835, 1994.
- [29] Chenyang Wu, Hui Bi, Bingchen Zhang, Yun Lin, and Wen Hong. L1 regularization recovered SAR images based interferometric sar imaging via complex approximated message passing. In *Image and Signal Processing for Remote Sensing XXIII*, volume 10427, page 1042717. International Society for Optics and Photonics, 2017.

- [30] Li Xi, Liu Guosui, and Jinlin Ni. Autofocusing of ISAR images based on entropy minimization. *IEEE Transactions on Aerospace and Electronic Systems*, 35(4):1240–1252, 1999.
- [31] Howard A Zebker, Charles L Werner, Paul A Rosen, and Scott Hensley. Accuracy of topographic maps derived from ers-1 interferometric radar. *IEEE Transactions on Geoscience and Remote Sensing*, 32(4):823–836, 1994.
- [32] O. Zengin and M. Çetin. Analysis of factors that impact the performance of sar interferometry. Technical report, Sabancı University, 2016.
- [33] O. Zengin and M. Çetin. Requirements for a DTED-II level interferometric SAR system. Technical report, Sabancı University, 2016.
- [34] Qun Zhao and Jose C Principe. Support vector machines for sar automatic target recognition. *IEEE Transactions on Aerospace and Electronic Systems*, 37(2):643–654, 2001.